Evaluation of a global total water level model in the presence of radiational S$_2$ tide

Pengcheng Wang [a],[*], Natacha B. Bernier [a], Keith R. Thompson [b], Tsubasa Kodaira [c]

[a] Recherche en Prévision Numérique Environnementale (RPN-E), Meteorological Research Division (MRD), Environment and Climate Change Canada, Dorval, Quebec, Canada
[b] Department of Oceanography, Dalhousie University, Halifax, Nova Scotia, Canada
[c] Department of Ocean Technology, Policy, and Environment Graduate School of Frontier Sciences, The university of Tokyo, Kashiwa, Japan

ARTICLE INFO

ABSTRACT

The development of a computationally efficient scheme for predicting the global distribution of total water level (TWL) is discussed. The ocean model is barotropic, has a horizontal grid spacing of 1/12°, and is based on the NEMO modeling framework. It is forced by the gravitational potential and hourly atmospheric fields for 2008. Hourly time spacing was required to resolve the S$_2$ tide in global air pressure and wind. The predicted tide in water deeper than 400 m was nudged to TPXO8 "observations" of tidal elevation or current using a scheme called tidal nudging (Kodaira et al., 2019). The benefit of nudging horizontal velocity in the momentum equation, compared to sea level in the continuity equation, is discussed. Tidal nudging is shown to improve tidal predictions of sea level at the coast, particularly at the S$_2$ tidal frequency. The predicted radiational S$_2$ tide in sea level forced solely by the S$_2$ tide in global air pressure reaches amplitudes exceeding 80 cm. Decreasing the time spacing of the air pressure forcing from 1 h to 3 h reduces the S$_2$ amplitude in air pressure by a factor of 0.82, consistent with expectations based on Fourier analysis. This highlights the importance of using hourly atmospheric forcing when predicting the global sea level response to atmospheric forcing. The radiational S$_2$ tide in sea level is subject to strong nonlinear interaction with the gravitational tide, leading to a pronounced attenuation of the radiational S$_2$ tide. The attenuation is explained by an increase in effective bottom friction at the S$_2$ frequency due to the presence of the gravitational tide. Four schemes for predicting TWL are evaluated to quantify the impact of tidal nudging and nonlinear interaction of tide and surge. Using TWLs observed by 304 coastal tide gauges, we show it is necessary to include both tidal nudging and nonlinear interaction. Plans for the further development of an operational flood forecast system for the Canadian coast, based on the above model, are discussed.

1. Introduction

Coastal flooding poses a major threat to coastal communities worldwide and its adverse impacts are expected to increase over the next century (e.g., IPCC, 2014; Hallegatte et al., 2013; Hinkel et al., 2014). An effective response to imminent coastal flooding requires a model that can accurately predict total water level (TWL) with lead times of hours to order ten days. There is also a need for decadal scale projections of probability distributions of TWL, and thus flooding risk, under plausible climate change scenarios. Both forecasting and projection applications require ensembles of runs and this increases the need for models that are computationally efficient.

One of the challenges in developing an accurate model of TWL is that the prediction of tide and surge, the dominant components of TWL for many coastal regions, is essentially a global problem. Furthermore, tides and surges at the coast are also influenced by local variations

in bathymetry through its effect on harbor and shelf-scale resonances, waveguides for coastal trapped waves, and tide-surge interaction. This wide range of spatial scales makes the choice of the grid spacing for the model critical. Although improvements in purely hydrodynamic (also referred to as "forward") global tidal models have been made through the inclusion of self-attraction and loading, and topographic internal wave drag (e.g., Kodaira et al., 2016b), further improvements are required to improve the parameterization of sub-grid scale processes.

It is well known that the oceanic tide can be excited by the atmospheric tide forced by the thermal effect of radiation, mostly at the solar diurnal (S$_1$) and semidiurnal (S$_2$) frequencies (e.g., Cartwright, 1978). The atmospherically-forced oceanic tides will henceforth be referred to as "radiational" tides (Munk and Cartwright, 1966) and denoted by rS$_1$ and rS$_2$. The amplitude of rS$_1$ is relatively small (∼1 cm) in contrast to the amplitude of rS$_2$ which can be 5–10 cm (Cartwright, 1978).

Similar to the gravitational S_2 tide, rS_2 is generated primarily over the tropical oceans and has a global response. As a result, rS_2 will be missed in regional flood forecasting systems if it is not included through the open boundary conditions. Furthermore, the atmospheric forcing for the ocean models must have sufficiently high temporal resolution in order to properly resolve rS_2 (Dobslaw and Thomas, 2005). Most operational and research flood forecasting systems are regional (e.g., Bernier and Thompson, 2015; Flowerdew et al., 2010; Werner et al., 2009; Allen et al., 2018) or global but with coarsely resolved (6 hour) atmospheric forcing (e.g., Carrère and Lyard, 2003; Verlaan et al., 2015). The present global study is the first to examine the effect of rS_2 on total water level forecasts using atmospheric forcing with a time spacing of one hour.

Coastal flooding is a major concern for Canadians. On the east coast, severe damage to coastal infrastructure and loss of life has been caused by flooding driven by hurricanes and strong winter storms (e.g., Bernier and Thompson, 2015; Danard et al., 2003). The most recent example is Hurricane Dorian. It made landfall just west of Halifax, Nova Scotia in 2019 and generated a surge level of about 1 m at Halifax and 1.6 m in Northumberland Strait, resulting in extensive flooding and severe damage to seawalls, houses and vessels. On the west coast of Canada, communities are also vulnerable to storm surges in winter and there is growing concern about the possibility of increasing storm frequency (Danard et al., 2003).

In the present study we evaluate several schemes for forecasting TWL for all of the Canadian coastline. In this study we will evaluate a global model that resolves important coastal wave guides (e.g., west and east coasts of North America) and the response to atmospheric S_2 forcing over the tropics. Global Ocean General Circulation Models with the capacity of predicting TWL have been developed (e.g., Schiller and Fiedler, 2007; Müller et al., 2010; Arbic et al., 2010, 2012). These earlier studies focused on the effect of tides on ocean circulation, or the joint simulation of barotropic and baroclinic tides, rather than TWL. Global models developed directly for TWL forecasting include the Global Tide and Surge Model (GTSM) developed by Verlaan et al. (2015) and the ADCIRC storm tide model developed by Pringle et al. (2021). Both models are barotropic and use unstructured spherical grids to provide a more detailed representation of coastal areas compared to the open ocean. The GTSM was used by Muis et al. (2016) for a global reanalysis of extreme sea levels. They only used the surge component of GTSM; tides were generated using the data-assimilative model known as FES2012 (Carrère et al., 2012) due to the weak performance of GTSM in tidal prediction at that time (Muis et al., 2016).

The main goal of the present study is the development of a computationally efficient scheme for accurately predicting the global distribution of TWL. This leads us to two questions of practical and scientific interest. The first question is how can we best predict tides using a model with limited spatial resolution? A simple approach would be to directly nudge the modeled tides toward tidal observations (e.g., Han et al., 2010; Fu et al., 2021). However, this approach is not suitable for TWL because the surge component of TWL will be suppressed by the nudging. In this study, we use a modified form of spectral nudging (Thompson et al., 2006) to target specific tidal frequency bands thereby reducing the suppression of the surges. Following Kodaira et al. (2019), we refer to this modified technique as "tidal nudging". The second question is what is the impact of neglecting tide-surge interaction (e.g., Bernier and Thompson, 2007; Davies and Lawrence, 1994; Horsburgh and Wilson, 2007) and tide–tide interaction on the prediction of TWL by a global model forced by hourly air pressure and wind stress?

The present study uses a $1/12°$ global barotropic model based on the Nucleus for European Modeling of the Ocean (NEMO) framework (Madec, 2008). The M_2 tide (Kodaira et al., 2016b) and surge (Kodaira et al., 2016a) components of this model have been separately validated and shown to be in reasonable agreement with global observations of the M_2 tide and surges. The model is further modified in the present study by including tidal nudging, and extending the southern limit of model grid to allow tidal propagation under ice shelves. The evaluation is carried out using hourly observations of TWL from a global array of 304 tide gauges for 2008. This year has the most surges exceeding 1 m in the global array of tide gauges since 2000.

The structure of the paper is as follows. The observations of coastal TWL, and tidal elevations and currents from the deep ocean, are described in Section 2. The ocean model, and its atmospheric forcing, are described in Section 3. The tide, surge and TWL predictions are evaluated in Section 4. The nonlinear interaction of rS_2 with the gravitational tide is also examined. The results are summarized and discussed in the final section.

2. Observations for model evaluation

Tidal elevations and currents from a data-assimilative model based on Egbert and Erofeeva (2002) are used for tidal nudging and model evaluation. Tidal amplitudes and phases for eight tidal constituents (M_2, S_2, N_2, K_2, O_1, K_1, P_1 and Q_1) were obtained from Oregon State University on a global grid with a spacing of $1/30°$. (These data will henceforth be referred to as TPXO8.) Given the good agreement between TPXO8 and amplitudes and phases calculated from independent observations (Stammer et al., 2014), TPXO8 will henceforth be treated as "observations".

Hourly TWLs observed by a global array of tide gauges were obtained from the University of Hawaii Sea Level Centre (UHSLC, Caldwell et al., 2015). All available data of research quality were downloaded for 2008. Stations were excluded if any of the following criteria were met: (1) the proportion of missing observations exceeds 90%; (2) the station is more than 25 km from the nearest ocean model grid point; (3) the station is shielded from the open ocean by barrier islands or located far inland on a river; (4) the station is on an island too small to be resolved by the model. Applying the four selection criteria resulted in a global distribution of 304 stations (Appendix A).

The global distribution of the 304 tide gauge stations is uneven and this causes difficulty when attempting to plot the global distribution of point statistics such as root mean square error (RMSE). For this reason the 304 stations were reordered taking into account the tendency of extended coastlines to act as wave guides for coastal trapped waves. The reordered station codes are listed in Appendix A and their locations, grouped by 8 subregions, are plotted in Fig. A.1. Several of the figures in this study show point statistics such as RMSE as a function of station number, grouped by subregion.

3. The ocean model

3.1. Governing equations

The model is based on the following depth-averaged barotropic momentum equation

$$\frac{\partial \boldsymbol{u}}{\partial t} + \boldsymbol{u} \cdot \nabla \boldsymbol{u} + \boldsymbol{f} \times \boldsymbol{u} = -g\nabla[(1 - \alpha_s)\eta - \eta_A] + A\nabla^2 \boldsymbol{u}$$
$$+ \frac{\boldsymbol{\tau}_s - \boldsymbol{\tau}_b}{\rho H} - \frac{1}{\rho}\nabla p_a - c_{iw}\boldsymbol{u} + \lambda(\boldsymbol{x})\langle \boldsymbol{u}_{obs} - \boldsymbol{u}\rangle \tag{1}$$

and continuity equation

$$\frac{\partial \eta}{\partial t} + \nabla \cdot (H\boldsymbol{u}) = 0 \tag{2}$$

where $\boldsymbol{u} = (u, v)$ is the depth-averaged horizontal velocity, $\boldsymbol{f}$ is the Coriolis parameter multiplied by the upward pointing unit vector, η is the sea surface height, η_A is the gravitational tidal potential, A is the horizontal viscosity, $\boldsymbol{\tau}_s$ and $\boldsymbol{\tau}_b$ are the surface and bottom stress, H is total water depth and p_a is atmospheric pressure at sea level. The coefficients α_s and c_{iw} parameterize self-attraction and loading, and topographic internal wave drag, respectively. We use the water depth dependent factor α_s derived empirically by Stepanov and Hughes (2004). The coefficient c_{iw} is calculated following the formulation of Jayne and

St. Laurent (2001). Its global distribution is given by Kodaira et al. (2016b).

The last term on the right side of (1) denotes the nudging of the model's current u toward the observed current u_{obs} given by TPXO8. The angle brackets represent temporal filtering of the nudging term to isolate variability in selected tidal frequency bands (Kodaira et al., 2019). $\lambda(x)$ determines the spatially varying strength of the nudging at horizontal position x. To allow surges, and nonlinear processes that cause tide-surge and tide–tide interaction (e.g., Davies and Lawrence, 1994; Le Provost, 1991), to evolve freely on the shelf, λ was set to zero in water shallower than 400 m. In deeper water $\lambda(x)$ increased with water depth to a maximum value of $0.05/\Delta$ where Δ is the baroclinic time step discussed below. The global distribution of $\lambda(x)$ is shown in Fig. 1. Spatial smoothing ensured a gradual transition of $\lambda(x)$ from deep to shallow water.

The tidal nudging methodology is further discussed in Appendix B. It is shown that tidal nudging of currents in the momentum equation is preferable to adding a sea level nudging term of the form $\lambda\langle\eta_{obs} - \eta\rangle$ to the right side of the continuity equation (2).

The governing equations are solved numerically using the NEMO modeling framework (Madec, 2008). The model grid is the extended version of a tri-polar ORCA grid (referred to as eORCA12). It has a nominal resolution of $1/12°$ at the equator. Compared to the original version of ORCA12, the eORCA12 grid has been extended southward from 77°S to 85°S in order to allow tidal propagation under Antarctic ice shelves. Such propagation is required for accurate tide predictions throughout the Southern Ocean and potentially the tropics (De Kleermaeker et al., 2017).

Sensitivity studies (Appendix C) show that a grid spacing of $1/4°$ is too coarse to predict tides and surges. Increasing the resolution to $1/12°$ gives acceptable tide and surge predictions on a global scale. Further increasing the resolution to $1/36°$ yields, as expected, local improvements in areas with bathymetric features poorly resolved by $1/12°$ grid. However, these improvements come at an approximately 16 fold increase in run time. Given the present interest in extended range ensemble forecasts of TWL, and decadal-scale projections of flooding risk, computational efficiency is a major consideration and the rest of the study will focus on results from the $1/12°$ model.

The bathymetry is derived from GEBCO_2014 (Weatherall et al., 2015). The minimum and maximum water depths are set at 10 m and 6000 m. Over ice cavities in the Antarctic, ice thickness has been removed and only the water column thickness has been used as the bathymetry data. The ice thickness is derived from the Bedmap products (Fretwell et al., 2013) and does not change with time. In addition, the bathymetry in Hudson Bay and on the Labrador and Newfoundland Shelf was adjusted based on bathymetric data kindly provided by F. Lyard (personal communication). This modification was necessary in order to obtain accurate tide predictions for these regions and the adjacent North Atlantic.

The model is 2D barotropic with one single vertical layer representing the water column. The model is run with a baroclinic time step of 180 s and a mode-splitting procedure is employed to solve the barotropic equations using a time step of 6 s. For computational efficiency, all unnecessary calls to subroutines related to vertical processes and tracers were removed. Tidal nudging was applied at every baroclinic time step. The quadratic bottom friction was parameterized using a constant drag coefficient of 2.5×10^{-3}. To account for the effect of ice cover in the Ross and Weddell Seas, atmospheric forcing was turned off over ice cavities and the bottom drag coefficient was doubled to take into account the top friction.

3.2. Atmospheric forcing

Gridded fields of atmospheric forcing were obtained from the Global Deterministic Reforecast System (GDRS, Gasset et al., 2021) developed

by Environment and Climate Change Canada (ECCC). The GDRS configurations are closely related to the control member of the operational Global Ensemble Prediction System (GEPS, Lin et al., 2016) at ECCC. The GDRS is used to produce hourly forecast with a grid spacing of approximately 39 km. Following Bernier and Thompson (2007), the magnitude of the wind stress is calculated using $c_d(W)W^2$ where W is the wind speed and c_d is a drag coefficient that equals 1.2×10^{-3} for wind speeds below 8 m s^{-1}, increasing linearly with W for higher wind speeds with a slope of 0.065×10^{-3} for every 1 m s^{-1} increase in W. This drag coefficient formulation is currently used by the regional surge forecast system run operationally by ECCC.

The GDRS runs are renewed every 12 h, and the forecast continues for 24 h for each run. Forecast hours 0 to 5 are discarded to avoid adjustments that result from initialization based on the ERA-Interim reanalysis of Dee et al. (2011). To concatenate the time sequence of GDRS reforecast fields of wind and air pressure, temporal blending is applied to forecast hours 6 through 10 as follows:

$$b(t_i) = \beta(t_i)a_o(t_i) + [1 - \beta(t_i)]a_n(t_i) \qquad 6 \le t_i \le 10 \qquad (3)$$

where $b(t_i)$ is the blended forecast for hour t_i, $a_o(t_i)$ and $a_n(t_i)$ denote the old and new forecasts at the same time, and $\beta(t_i)$ is the blending coefficient defined by

$$\beta(6) = 0.50 \quad \beta(7) = 0.35 \quad \beta(8) = 0.25 \quad \beta(9) = 0.15 \quad \beta(10) = 0.05$$

The forecasts and the blending are performed every 12 h. The same blending procedure was used by Bernier and Thompson (2015) and Kodaira et al. (2016a).

The atmospheric forcing has a significant S$_2$ tide (Fig. 2). The S$_2$ tide in the GDRS hourly air pressures is strongest in the tropics where it reaches a maximum amplitude of 1.24 hPa in the eastern Pacific, consistent with observations (see Figure 8 of Dai and Wang, 1999). This well known semi-diurnal variation is due to the thermal effect of solar radiation (e.g., Lindzen and Chapman, 1969). The S$_2$ tide in the hourly GDRS winds is relatively small near the equator and increases poleward reaching speeds of 0.2 m s^{-1}. In the momentum equation (1), the direct contributions of air pressure and wind are expressed by the terms $\rho^{-1}\nabla p_a$ and $\rho^{-1}\tau_s/H$, respectively. Following Ray and Egbert (2004), the scaling of these two terms shows that, locally, the pressure term is at least two orders of magnitude larger than the wind stress term. This suggests that air pressure loading is the primary mechanism for exciting the S$_2$ tide in the ocean.

4. Results

Seven model runs are described and compared in this section. Each model run starts on November 8, 2007 and finishes on December 31, 2008. The output was stored hourly. To allow for model spin up, and also focus on the year 2008, the output for the last 54 days in 2007 was discarded. We note that a spin up time of 30–40 days, determined mainly by the spin up time of the tidal filter (see Appendix B), should be sufficient for the present study. This was confirmed by sensitivity studies using different spin up times.

To study the dynamical origin of the S$_2$ signal in the ocean, least squares is used to decompose the time-varying atmospheric forcing and ocean response at each grid point into a purely sinusoidal component with a period of 12 hours and a residual. For sea level at a given grid point, the decomposition takes the form

$$\eta(t) = \bar{\eta}(t) + \eta'(t) \qquad (4)$$

Similar decompositions can be written for $u(t)$, $p_a(t)$ and $\tau_s(t)$.

The first group of runs is subject only to gravitational forcing (Run$_T$, Run$_{Tn}$, Run$_{Tn}^*$). The second group (Run$_S$, Run$_{S'}$) is atmospherically forced and tidal nudging is set to zero. Run$_{S'}$ is forced by $p_a'(t)$ and $\tau_s'(t)$. The last group of runs (Run$_{TS}$, Run$_{TnS}$) allows for tide-surge and tide–tide interaction in the prediction of TWL, both with and without tidal nudging. The seven runs are summarized in Table 1.
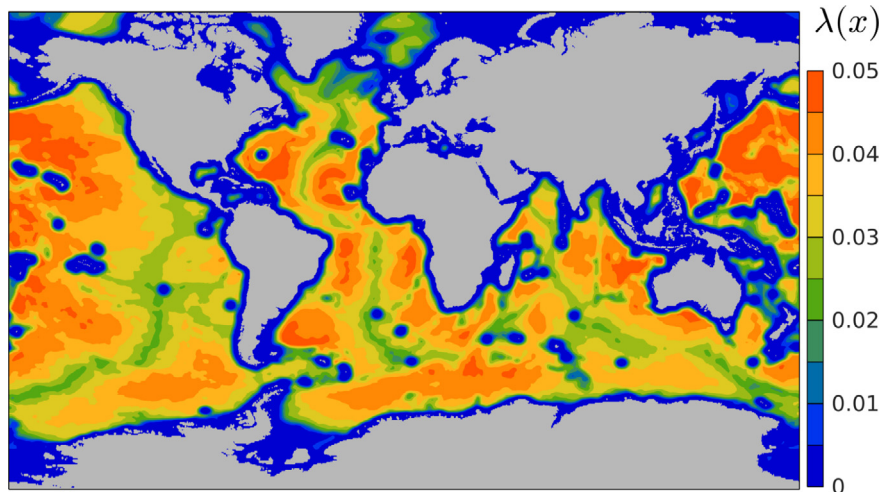
Fig. 1. Spatial distribution of the nudging coefficient. Units are $1/\Delta$ where Δ is the baroclinic time step (see Section 3.1).
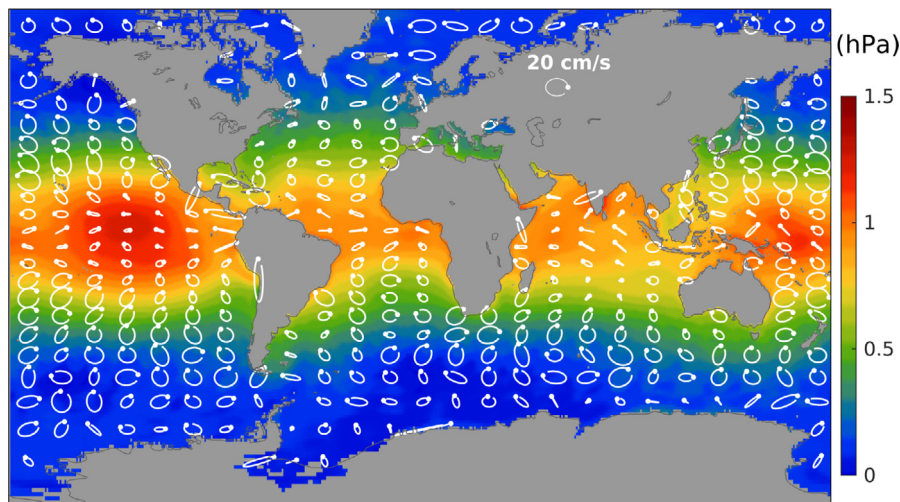
Fig. 2. Amplitude of the S_2 tide in atmospheric pressure (hPa, color shading) and wind (ellipses). Calculated from hourly GDRS data for 2008. The dot for each ellipse denotes a common start time and the last 1/12 of each ellipse is omitted to indicate sense of rotation.

Table 1

Design of the model experiments. Checkmarks indicate the forcing and the form of tidal nudging (if any). η_A refers to gravitational forcing. (τ_s, p_a) refers to forcing by hourly wind stress and air pressure and (τ'_s, p'_a) refers to atmospheric forcing with the S_2 component removed by least squares (see Eq. (4)). $\lambda \langle u_{obs} - u \rangle$ and $\lambda \langle \eta_{obs} - \eta \rangle$ refer to tidal nudging of u in the momentum equation, and η in the continuity equation, respectively.

	η_A	(τ_s, p_a)	(τ'_s, p'_a)	$\lambda \langle u_{obs} - u \rangle$	$\lambda \langle \eta_{obs} - \eta \rangle$
Run_T	✓				
Run_{Tn}	✓			✓	
Run^*_{Tn}	✓				✓
Run_S		✓			
$\text{Run}_{S'}$			✓		
Run_{TS}	✓	✓			
Run_{TnS}	✓	✓			✓

Comparison of these runs, both within and between groups, allows us to address the following questions: What is the impact of tidal nudging in the deep ocean on TWL predicted at the coast? Which variable, u or η, should be nudged? What is the impact of neglecting nonlinear tide-surge and tide–tide interaction on the prediction of TWL?

To assess model performance at each tide gauge we calculate the root mean square error (RMSE) from the difference of time series of observations and predictions. For reference, we also calculated the root mean square (RMS) of observations for the same period for each tide gauge. To facilitate the comparison with different scales, we also use the γ^2 statistic of Thompson and Sheng (1997):

$$\gamma^2 = \frac{Var(O - M)}{Var(O)} \tag{5}$$

where Var denotes variance, and O and M denote observation and model simulation respectively. Small values of γ^2 indicate good model performance. If $\gamma^2 > 1$, the model simulations are worse than using the mean of the observations as a predictor.

4.1. Predicting the tides

It was shown in Appendix B that tidal nudging in deep water (Fig. 1) improves predictions of M_2 tidal elevation at the coast. In this subsection we extend the model evaluation to include the following tidal constituents: M_2, S_2, N_2, K_2, O_1, K_1, P_1 and Q_1. The harmonic analysis was performed using the T_TIDE package of Pawlowicz et al. (2002). Given a complete hourly record for all of 2008, the tidal package will select 68 tidal constituents. Given a six month record the tidal analysis will resolve all eight constituents included in the gravitational forcing of the ocean model. For this reason we focused this evaluation on 289 out of the 304 tide gauges with at most 50% missing observations
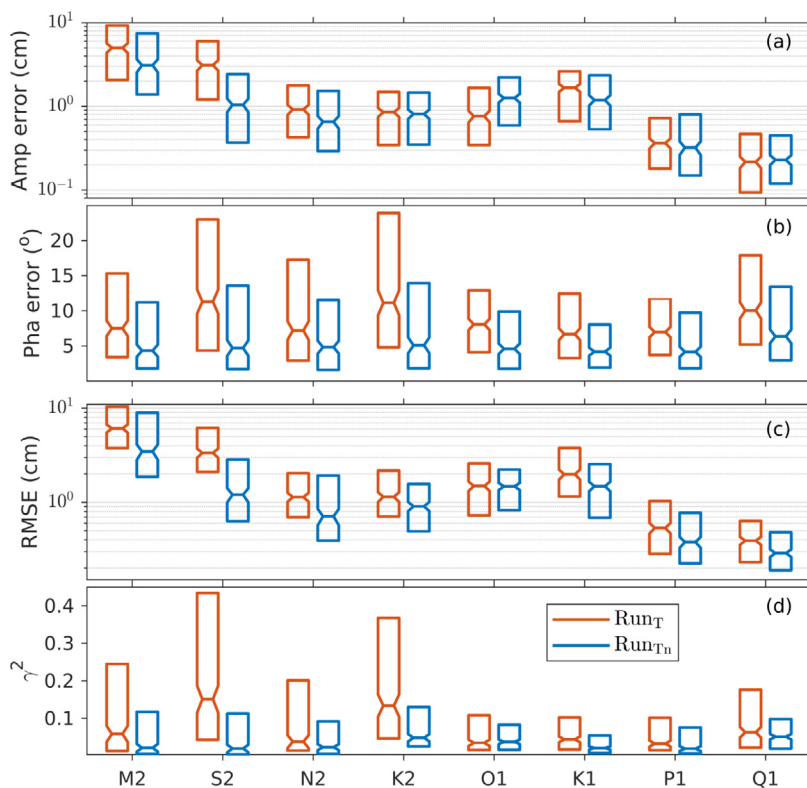
Fig. 3. Box plots, showing the three quartiles only, of the (a) amplitude errors, (b) phase errors, (c) RMSE and (d) γ^2 for the 8 major tidal constituents. The narrowest part of the notch indicates the median and the limits of the notch indicate the 95% confidence interval.

for 2008. For the tidal analysis of observed and predicted time series, missing values in the observations were also treated as missing in the predictions.

To provide a global assessment of skill, we use box plots (Fig. 3) to present the three quartiles of the error metrics across all 289 stations for a given run and a given tidal constituent. Box plots of amplitude and phase errors are shown in Fig. 3a and b. Comparison of Run_T and Run_{Tn} shows that tidal nudging effectively reduces all three quartiles of amplitude errors for M_2, S_2, N_2, and K_1, but increases the three quartiles for O_1 (Fig. 3a). The effect of tidal nudging on the amplitudes of K_2, P_1 and Q_1 is insignificant. The tidal nudging is however more consistent in correcting the phase errors by reducing the three quartiles for all eight constituents (Fig. 3b).

Box plots of RMSE and γ^2, taking into account both amplitude and phase errors, are further shown in Fig. 3c and d. The tidal nudging reduces the three quartiles of both error metrics for all constituents, except for O_1 where the overall effect of tidal nudging is relatively neutral. The reductions are largest for the semi-diurnal constituents, and most dramatic for S_2 where the second quartile, for example, is reduced by 54% for RMSE and 87% for γ^2. One reason for this large drop is that Run_{Tn} includes the radiational S_2 tide through the nudging to TPXO8 which includes rS_2 because it assimilates altimetry data. Given the TWL observations include this rS_2 signal, nudging to TPXO8 favors Run_{Tn} over Run_T at the S_2 tidal frequency.

Individual values of RMS, RMSE and γ^2 for the 289 tide gauges are shown in Fig. 4. All eight tidal constituents were used to reconstruct the tides. The RMSE for Run_{Tn} is mapped in Fig. 4a, and the difference in RMSE for Run_T and Run_{Tn} is mapped in Fig. 4b. RMS, RMSE and γ^2 are plotted as a function of station code in Fig. 4c and d. (The ordering and grouping of the stations is described in Appendix A.) It is encouraging to note that tidal nudging reduces the RMSE at 82% of the stations. Fig. 4b and c show relatively large improvements to the northwest of Australia (0.21–0.54 m, station codes 194–196) and in the Gulf of Maine (0.15–0.28 m, station codes 99–101) where the tidal

range is large. Degradation of skill occurs at 18% of the stations but we note that the degradation is typically less than 0.05 m.

Fig. 4d further shows that tidal nudging effectively reduces γ^2 values at most stations regardless of the tidal range. $\gamma^2 < 1$ for Run_{Tn} occurs at 97% of the stations indicating the model has skill. Large γ^2 values (greater than 2) are seen at stations in the Baltic Sea (station codes 111–114) due mainly to the fact that observed tidal signals are very weak there (RMS < 6 cm). γ^2 slightly greater than unity is also found for Woods Hole (station code 98), the west coast of Florida (station codes 83–84), and the eastern side of the Strait of Malacca (station codes 158–160). We speculate that the poor performance of Run_{Tn} at these stations could be improved by increasing model resolution.

The performance of the nudged run is comparable to the altimeter constrained FES2012 tidal model. Muis et al. (2016) obtained an arithmetic mean of RMSE of 0.15 m based on a multidecadal run of FES2012. The arithmetic mean of RMSE for Run_{Tn} in this study is 0.10 m but it is important to note that the tide gauges, and the analysis period, used in the present study differ from those of Muis et al. (2016).

4.2. Predicting the surges

We now examine the response of the ocean to atmospheric forcing. Both gravitational forcing and tidal nudging are set to zero. The initial focus is on the response to $\tilde{p}_a(t)$, i.e., forcing by air pressure at the S_2 tidal frequency. This is followed by an examination of the ocean response to the full atmospheric forcing, $p_a(t)$ and $\tau_s(t)$. (See Eq. (4) for the decomposition of forcing and response into a component proportional to S_2 and a residual.)

4.2.1. Sea level response to $\tilde{p}_a$ and need for hourly forcing

The global response of sea level at the S_2 tidal frequency to forcing by the S_2 tide in the hourly air pressure (Figs. 5a or 2) is shown in Fig. 5b. The maximum amplitude (88 cm) is found in the Bristol Channel and the second largest (71 cm) in the Bay of Fundy. These
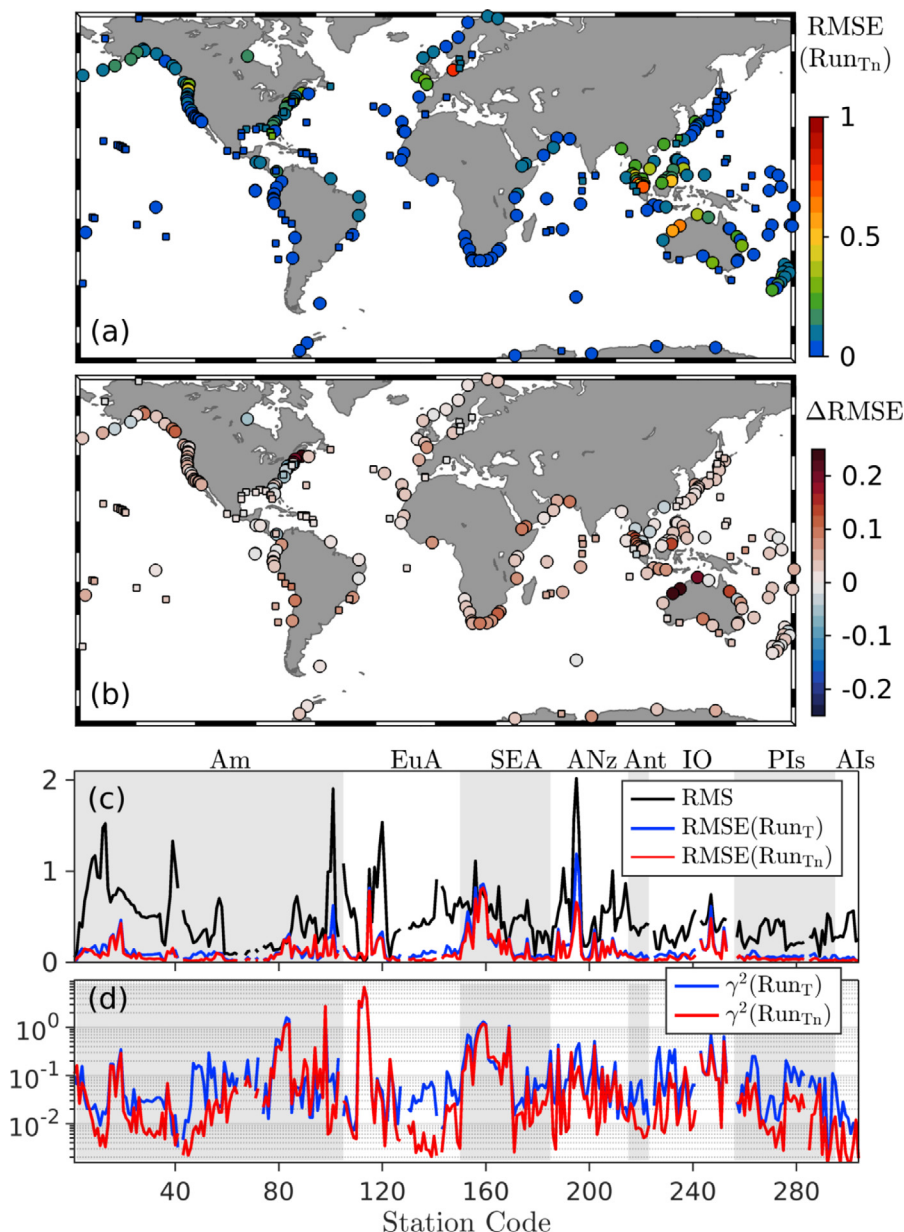
Fig. 4. Fit to the observed tide. (a) RMSE for the nudged run, Run_{Tn}. (b) The difference in RMSE between the un-nudged to nudged runs, Run_T-Run_{Tn}. In (a) and (b), squares show locations with RMS of observed tide below 0.3 m. (c) RMS of observed tide (black) and the RMSE for Run_T (blue) and Run_{Tn} (red) as a function of station code (Appendix A). (d) γ^2 for Run_T and Run_{Tn} as a function of station code. All RMS and RMSE values in m.

values are much larger than the amplitudes predicted by the inverse barometer effect which are everywhere less than 2 cm (Fig. 5a). The spatial pattern of the amplitude is similar to that of the gravitational S_2 tide (Arbic, 2005), and both can be explained in terms of excitation of oceanic normal modes by forcing at the S_2 frequency (Platzman et al., 1981; Arbic, 2005).

Dobslaw and Thomas (2005) compared the response of the global ocean to $\tilde{p}_a$ using air pressure forcing calculated from analysis fields defined every 6 h and forecast fields defined every 3 h. Linear interpolation was used to map the pressure fields to the time step of the ocean model. Dobslaw and Thomas (2005) found a large difference in the ocean response on switching from 3 h to 6 h forcing. The main reason is 6 h forcing can only resolve a standing wave in contrast to 3 h forcing which can capture propagation.

Building on the study of Dobslaw and Thomas (2005), we repeated our calculation of the ocean response to $\tilde{p}_a$ with one change; we subsampled the hourly GDRS pressure fields to 3 h and then linearly interpolated back to hourly values. The results are shown in Fig. 5c and d. The amplitude of $\tilde{p}_a$ (Fig. 5c and a) for 3 h sampling is similar to the amplitude pattern for 1 h sampling apart from a reduction by a factor of about 0.82. (This factor was obtained by regression of the 3 h amplitudes on the 1 h amplitudes.) The reduction can be explained by considering a sinusoid with a period of 12 h defined in discrete time with a sampling interval of 1 h. If the sinusoid is subsampled every 3 h and then linearly interpolated back to hourly values, the amplitude of the Fourier coefficient at a period of 12 h is reduced by 0.829. For completeness Fig. 5e and f show the effect of subsampling the hourly p_a forcing every 6 h. It differs greatly from the response to 1 h and 3 h forcing for the reasons given by Dobslaw and Thomas (2005).

The amplitude of the sea level response to 1 h and 3 h pressure forcing (Fig. 5b and d) are, as expected, quite similar. The sea level response to 3 h forcing is reduced by a factor of about 0.75 (again based on regression of the 3 h amplitudes on the 1 h amplitudes). The reason for the deviation from the theoretical value of 0.829 is presumably
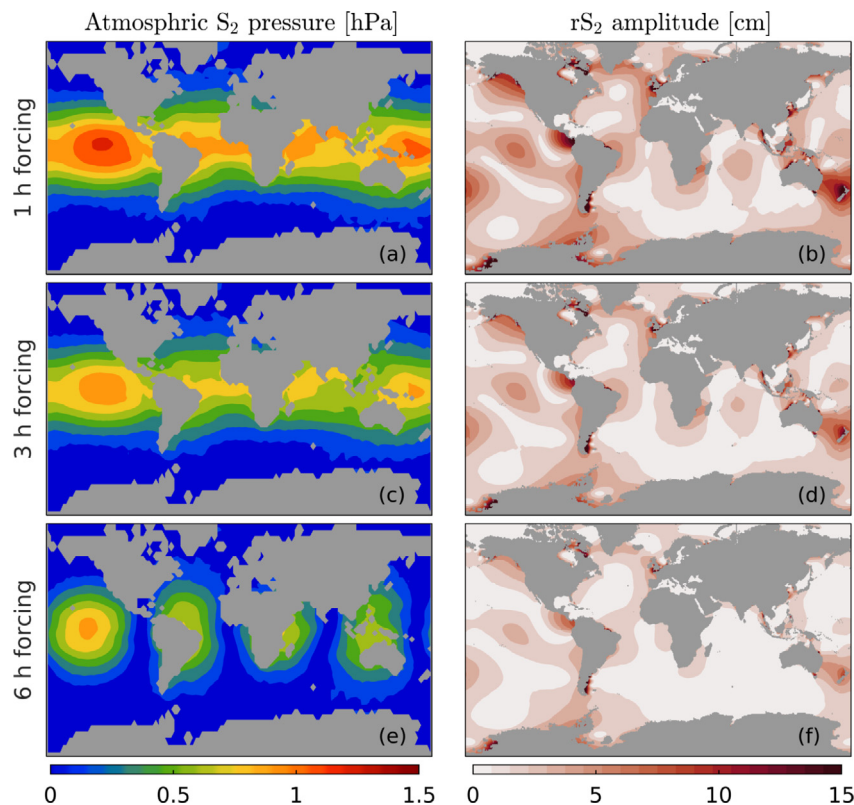
Fig. 5. Amplitude of the S_2 tide in air pressure ($\bar{p}_a$, left panels) and the associated radiational S_2 tide in sea level (right panels). The air pressure forcing for the top row is calculated using hourly GDRS reforecast fields for 2008. The middle and bottom rows result from subsampling the hourly pressure fields every 3 and 6 hours and linearly interpolating back to hourly values.

due to the effect of model nonlinearities on the ocean response. The maximum amplitude is still found in the Bristol Channel but the value is reduced from 88 cm to 73 cm. For completeness we also include the ocean response to 6 h forcing (Fig. 5f).

4.2.2. Sea level response to hourly forcing by (p'_a, τ'_s) and (p_a, τ_s)

We now examine the response to forcing by hourly variations in air pressure and wind stress. Gravitational forcing and tidal nudging are both set to zero. The full tidal signal, including S_2, was removed from the 304 observed TWL records using the T_TIDE package of Pawlowicz et al. (2002). The residuals from this tidal analysis are used for model evaluation.

For the evaluation of the surge predictions we follow Kodaira et al. (2016a) and apply a high pass Butterworth filter to the observed residual and predicted sea level time series to suppress variability with periods $T_p > 20$ days. This was done to exclude low frequency baroclinic variability that cannot be predicted by the barotropic ocean model.

We first examine $\text{Run}_{S'}$ which is forced by air pressure and wind stress with the S_2 component removed, (p'_a, τ'_s). To quantify fit we initially focus on γ^2 (Fig. 6d) which takes into account both RMSE and RMS of observations. Reasonable model skill is found for 161 stations outside the tropics where the three quartiles of γ^2 are 0.24, 0.34 and 0.47. (Tropical stations are defined as stations located between 23.4° North and 23.4° South. See Table A.1 for latitudes of all stations.) The model skill for the 143 tropical stations is relatively low with γ^2 close to unity for most stations (Fig. 6d): the three quartiles of γ^2 are 0.83, 0.98 and 1.11. This is not surprising because surges are small at most tropical island locations (Fig. 6c) and model resolution is also an issue. We also speculate that higher resolution atmospheric forcing is required to better capture the effect of tropical cyclones at these stations.

We now focus on Run_S which is forced by the unmodified atmospheric forcing, (p_a, τ_s). The change in RMSE at each tide gauge is

mapped in Fig. 6b. The Run_S predictions includes rS_2 and so it is not surprising that RMSE increases on replacing (p'_a, τ'_s) by (p_a, τ_s). The largest increases occur in regions with large rS_2 (Fig. 5b). These regions include the Gulf of Alaska, Northwest European Shelf, Strait of Malacca, northwest coast of Australia, and New Zealand. The difference in surge response predicted by Run_S and $\text{Run}_{S'}$ is illustrated in Fig. 7 for three tide gauges. At Cuxhaven on the Northwest European shelf, the amplitude of the S_2 signal in the Run_S predictions reaches amplitudes of 0.5 m. At nearby Brest and Taranaki (New Zealand) the amplitudes reach 0.2 m.

Taylor diagrams (Taylor, 2001) for Run_S and $\text{Run}_{S'}$ are shown in Fig. 8. We have modified the Taylor diagram by adding a line (green semi-circle in Fig. 8) that shows, for positive correlation, the minimum RMSE that could be achieved by optimally scaling the predictions, i.e., sliding a point radially to the point of minimum RMSE. These diagrams confirm that removing the S_2 tide from the atmospheric forcing leads to more accurate surge predictions, particularly outside the tropics. They also highlight the danger of running a global surge prediction model with uncorrected hourly atmospheric forcing (Run_S).

4.2.3. Damping of the radiational s_2 tide by the gravitational tide

The S_2 amplitudes of sea level calculated using hourly forcing (Fig. 5b) agree qualitatively with results from previous studies (e.g., Fig. 1b of Arbic, 2005; Fig. 2 of Dobslaw and Thomas, 2005; Fig. 5b of Williams et al., 2018). Our amplitudes are however generally larger. The discrepancy is explained by the nonlinear interaction of the S_2 radiational and gravitational tide. Fig. 5 is based on atmospheric forcing only, in contrast to the results shown in the above mentioned studies which arise from differences in coupled tide-surge runs and tide-only runs. Fig. 9a and b show the amplitude of S_2 tidal elevation derived from the surge-only run (Run_S) and the differences between the coupled tide-surge run and tide-only runs (Run_{TS} - Run_T). The difference in the S_2 amplitude maps (Fig. 9c) shows clearly that
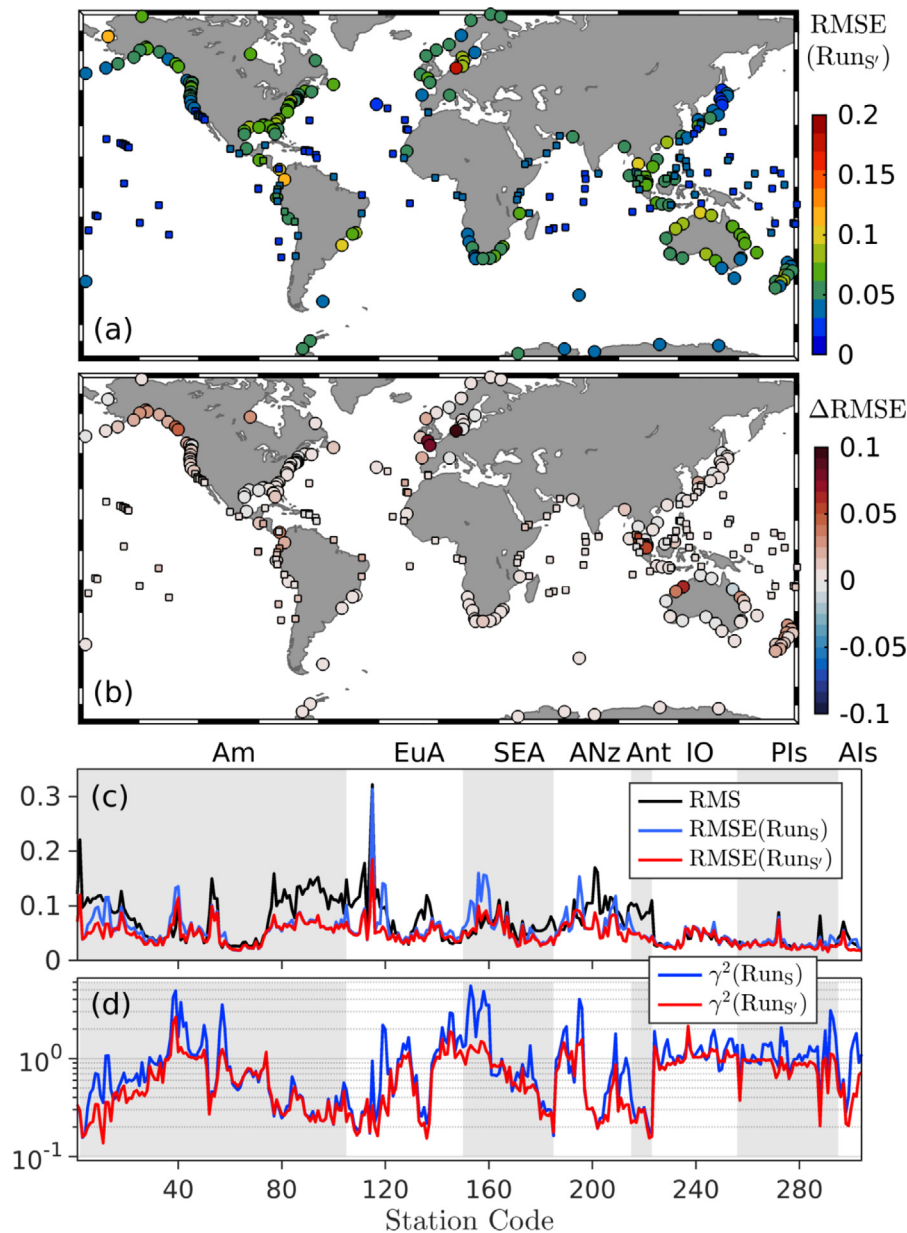
Fig. 6. Fit to the observed tidal residual. (a) RMSE for run forced by (p'_a, τ'_s), $Run_{S'}$. (b) The difference in RMSE for Run_S-$Run_{S'}$. In (a–b), squares show locations with RMS of observed residual below 5 cm. (c) RMS of observed residual (black) and RMSE for Run_S (blue) and $Run_{S'}$ (red) as a function of station code (Appendix A). (d) γ^2 for Run_S and $Run_{S'}$ as a function of station code. All RMS and RMSE values in m.

nonlinear interaction reduces the S_2 amplitudes from the surge only run by order 10 cm in some regions (e.g., southern North Sea, the Patagonia Shelf and the Ross Sea). We note however that larger reductions can be found, e.g., up to 80 cm in the Bristol Channel, 53 cm on the Patagonia Shelf and 28 cm in the Strait of Malacca.

It is well known that the quadratic bottom friction term in (1) is an important cause of tide-surge and tide–tide interaction. It is also well known that if a time varying current $\mathbf{u}(t)$ is a linear combination of tidal components then the contribution of $\mathbf{u}|\mathbf{u}|$ at a given tidal frequency will be increased by the variability associated with the other tidal components (Heaps, 1978; Inoue and Garrett, 2007). Inoue and Garrett (2007) showed that minor tidal constituents experience proportionately more friction than the dominant constituents.

To physically explain the difference in S_2 amplitudes from Run_S and Run_{TS} - Run_T (Fig. 9c), we extracted the time-varying bottom stress from Run_S, and the difference in bottom stress from Run_{TS} and Run_T, at each grid point. We then estimated the complex S_2 amplitude of

these two time-varying vector quantities and used their magnitude as a metric for the "strength" of bottom stress at the S_2 frequency. Fig. 9d shows the ratio of the metrics for Run_{TS} - Run_T and Run_S. This figure shows that the inclusion of gravitational tidal forcing in a global surge model can increase bottom friction at the S_2 frequency by a factor of about 10 in some regions (e.g., southern North Sea, the Patagonia Shelf, and the Ross Sea). Given the similarity of Fig. 9c and d, we conclude that enhancement of bottom friction by the gravitational tide is the major cause of the damping of the radiational S_2 tide in the coupled tide-surge run.

4.3. Predicting total water level

We now evaluate four ways of predicting TWL based on the model runs listed in Table 1. Model predictions are compared with observations of hourly TWL recorded during 2008 at the 304 stations listed in Table A.1. In addition to errors in the atmospheric forcing, it is
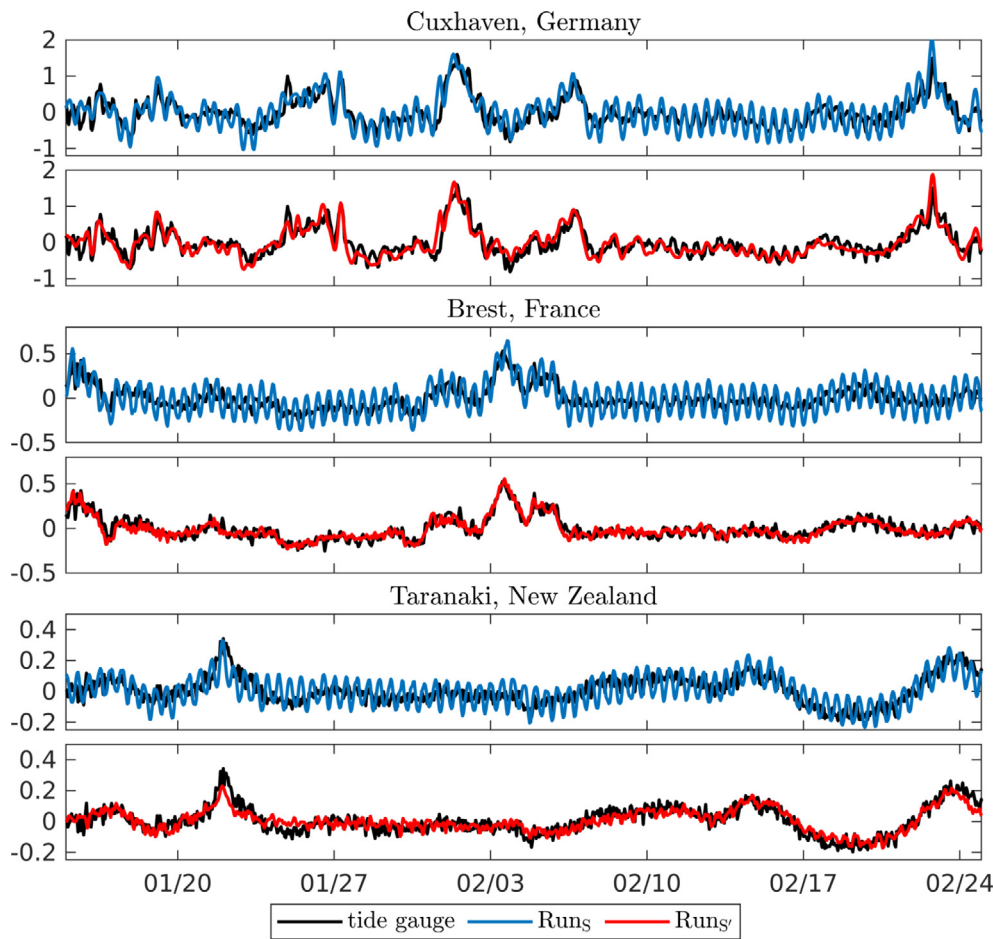
Fig. 7. Time series of observed residual (black) and predicted surge from Run_S (blue) and $Run_{S'}$ (red) at three tide gauges for the period January 15, 2008 to February 24, 2008. All values in m.

important to note that the observed TWLs are influenced by factors not captured by the ocean model including (i) baroclinicity on multiple time scales including its contribution to the low frequency annual and semi-annual tides, Sa and Ssa (ii) semi-diurnal and diurnal tidal constituents other than the eight included in the model (i.e., M_2, S_2, N_2, K_2, O_1, K_1, P_1, Q_1) (iii) bay and harbor seiches with periods of several hours caused by small scale variations in coastline and bathymetry. These discrepancies motivated us to compare the observed and predicted TWL times series in several frequency bands as detailed below.

An overall evaluation of the four prediction schemes in four frequency bands is given by box plots showing the three quartiles of RMSE and γ^2 (Fig. 10a and b). Two schemes are based on the un-nudged form of the tidal model ($\lambda = 0$ everywhere). Run_T+Run_S refers to the sum of separate predictions by the un-nudged tidal run (Run_T) and the surge run (Run_S). Run_{TS} includes tide-surge interaction (Table 1). The remaining two schemes are similar to Run_T+Run_S and Run_{TS} but they both use tidal nudging ($Run_{Tn}+Run_S$ and Run_{TnS} respectively).

Overall, Run_T+Run_S provides the least accurate predictions of TWL across all frequency bands based on the three quartiles of RMSE and γ^2 (Fig. 10a and b). This is to be expected because Run_T+Run_S does not include tidal nudging (Section 4.1) or the nonlinear interaction that damps the unrealistically large radiational S_2 tide predicted by Run_S (Section 4.2.3).

Allowing for tide-surge interaction (Run_{TS}) leads to a modest reduction of the three quartiles of RMSE and γ^2 (Fig. 10a and b). The reductions can be much larger on a local scale. For example, the largest RMSE reduction (0.09 m) is found at Cuxhaven. RMSE reductions in excess of 0.03 m are found at 12 additional stations, all from regions with high radiational S_2 tide (Fig. 5b): stations 119, 120 on the Northwest

European Shelf; 153, 156, 158–160 from the Strait of Malacca; 8, 9, 12, 13 from Alaska and British Columbia; 39 from the Pacific coast of Panama. Fourier analysis shows the difference between Run_T+Run_S and Run_{TS} is dominated by variability with a period of 12 hours. This leads us to conclude that the largest reductions in RMSE of Run_{TS} relative to Run_T+Run_S is due to gravitational tidal damping of the radiational S_2 tide.

$Run_{Tn}+Run_S$ is the sum of the tidally-nudged and surge-only runs. It outperforms Run_T+Run_S and Run_{TS} based on the quartiles of RMSE and γ^2 (Fig. 10a and b). The improvement is due entirely to nudging the tides toward the TPXO8 tidal observations in deep water (Section 4.1). One of the issues with $Run_{Tn}+Run_S$ is that it leads to double counting of the radiational S_2 tide because both Run_{Tn} and Run_S contain an rS_2 signal. Another issue is that, as with Run_T+Run_S, $Run_{Tn}+Run_S$ will overestimate rS_2 due to lack of gravitational damping. We will not discuss this TWL prediction scheme further.

Run_{TnS} includes tidal nudging and tide-surge interaction. Its quartiles of both RMSE and γ^2 are the lowest for all prediction schemes across all four frequency bands. The individual RMSE values are mapped in Fig. 11a. RMSE and γ^2 are also plotted by station code in Fig. 11b and c. They are all listed for each station in Table A.1. There is generally good agreement between the observed and predicted TWL with the RMSE below 0.20 m for 83% of the stations, and $\gamma^2 < 1$ for 99% of the stations. Relatively large γ^2 values are found for Woods Hole (station code 98) and the eastern side of the Strait of Malacca (station codes 158–160); they can be explained by tide prediction errors (compare Figs. 11c and 4d and see discussion in Section 4.1). Muis et al. (2016) reported an arithmetic mean of RMSE of 0.17 m for their global tide and surge model reanalysis. Our arithmetic mean of RMSE
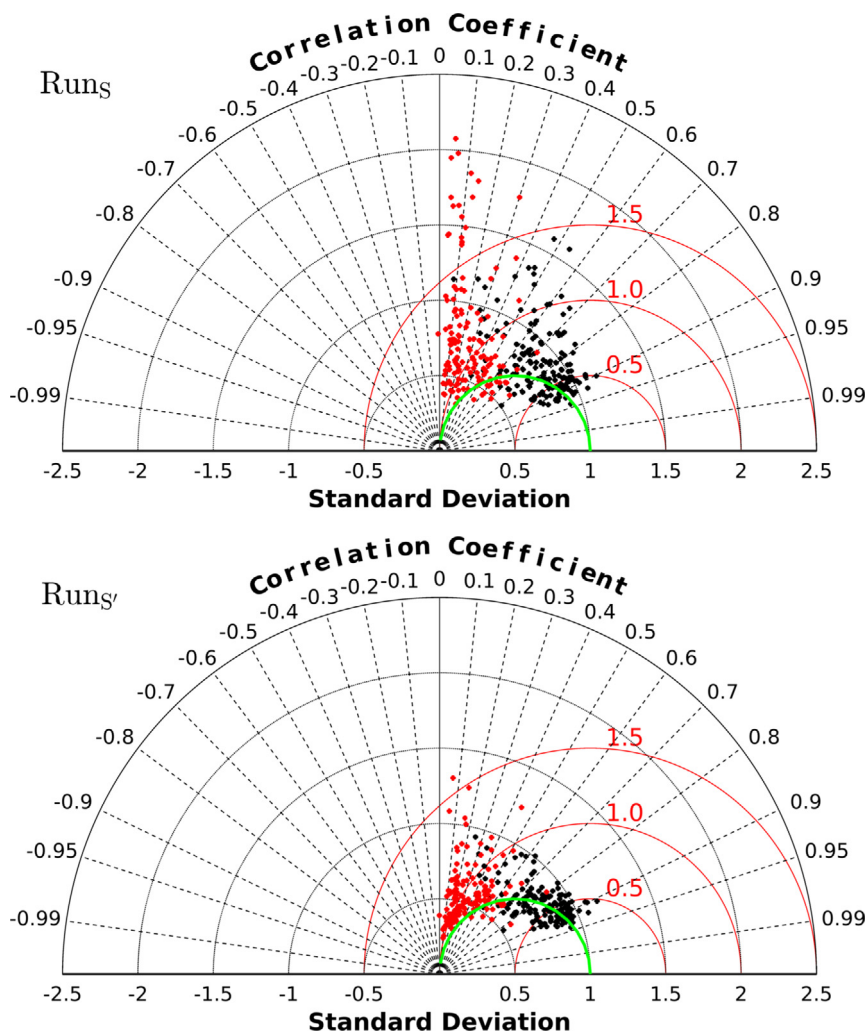
Fig. 8. Taylor diagrams for Run$_S$ (upper panel) and Run$_{S'}$ (lower panel). Each dot corresponds to a tide gauge station (Table A.1). Red dots indicate stations in the tropics. For each station, the observations and predictions are normalized by the standard deviation of the observations. Distance of each point from $(0,0)$ is the normalized standard deviation of the predictions. Distance from $(1,0)$ is the normalized standard deviation of the difference between observations and predictions (RMSE). The azimuthal angle indicates the correlation between observations and predictions. The green semi-circle shows, for positive correlation, the minimum RMSE that can be achieved by optimally scaling the predictions.

for Run$_{TnS}$ is 0.15 m although we caution that the study period and selection of tide gauges differ.

Fig. 10c summarizes the relative performance of the four schemes. For unfiltered TWL times series (first group), Run$_{TnS}$ has the lowest RMSE or γ^2 for 195 out of the total of 304 tide gauges. By way of contrast Run$_T$+Run$_S$ has the lowest RMSE or γ^2 at only 20 gauges. For the semi-diurnal frequency band (periods between 16 and 9.6 hours), Run$_{TnS}$ has the lowest RMSE or γ^2 for 210 gauges. This bar graph clearly shows that Run$_{TnS}$ has the best overall performance.

5. Summary and conclusions

The present study focuses on the development of a computationally efficient scheme for accurately predicting the global distribution of TWL. Two overriding questions were addressed: What is the best way to predict tidal elevation at the coast using an operational model with limited spatial resolution? What is the impact of neglecting nonlinear tide-surge and tide–tide interaction?

The underlying model is based on the NEMO modeling framework. On the basis of a set of sensitivity runs (Appendix C), we chose a horizontal grid spacing of $1/12°$ as a compromise between model accuracy and computational efficiency. The model was forced by air pressure and wind reforecast fields for 2008 provided by ECCC with

a time spacing of one hour. This relatively high temporal resolution allowed us to resolve the S_2 tide in global air pressure and wind.

The predicted tide in water deeper than 400 m (Fig. 1) was nudged to TPXO8 "observations" of tidal elevation or current using a scheme called tidal nudging (Kodaira et al., 2019). The idea is to restrict the nudging to specified tidal bands. The width of the nudged frequency bands is controlled by a single parameter, κ. The approach is conceptually similar to applying a conventional tidal analysis over a sliding window; increasing κ is equivalent to reducing the width of the window. In contrast to Kodaira et al. (2019) who nudged η in the continuity equation, we nudged u in the momentum equation. This resulted in more accurate predictions of u leading to dynamically consistent improvements in η through the continuity equation. Nudging u also avoids violation of the continuity equation which is a major drawback of nudging η (Appendix B). As expected, tidal nudging improves the tidal predictions in deep water where it is applied. Based on comparisons with independent TWL observations made by 304 tide gauges, the nudging also improves tidal predictions at the coast. More specifically, the nudging improves the tidal predictions at 82% of the tide gauges and decreases the arithmetic mean of RMSE across all gauges by 23% (from 0.13 to 0.10 m).

The radiational S_2 tide in sea level forced solely by the S_2 tide in global air pressure reached amplitudes exceeding 80 cm. In accord with previous studies, we found that forcing over the tropics is most effective
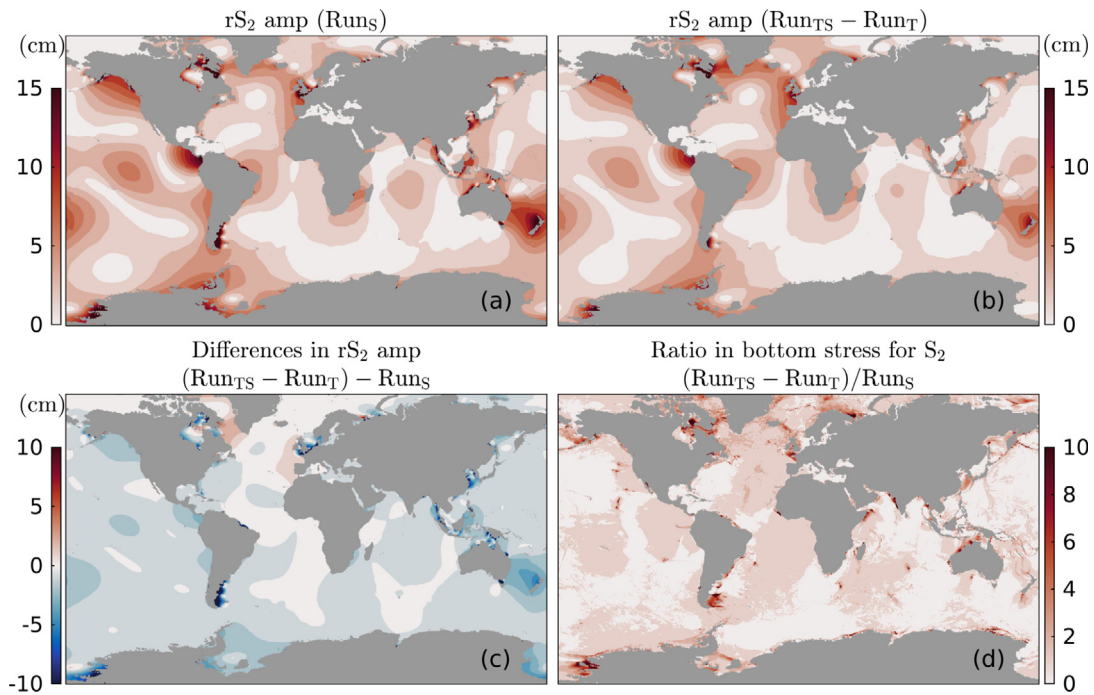
Fig. 9. Amplitude of radiational S_2 and the influence of gravitational damping. Amplitude of S_2 tidal elevation derived from (a) Run_S and (b) Run_{TS} - Run_T, and (c) the difference in S_2 amplitudes presented in (a) and (b). (d) The ratio of bottom stress at the S_2 tidal frequency calculated from Run_{TS} - Run_T and Run_S. All S_2 amplitudes in cm.
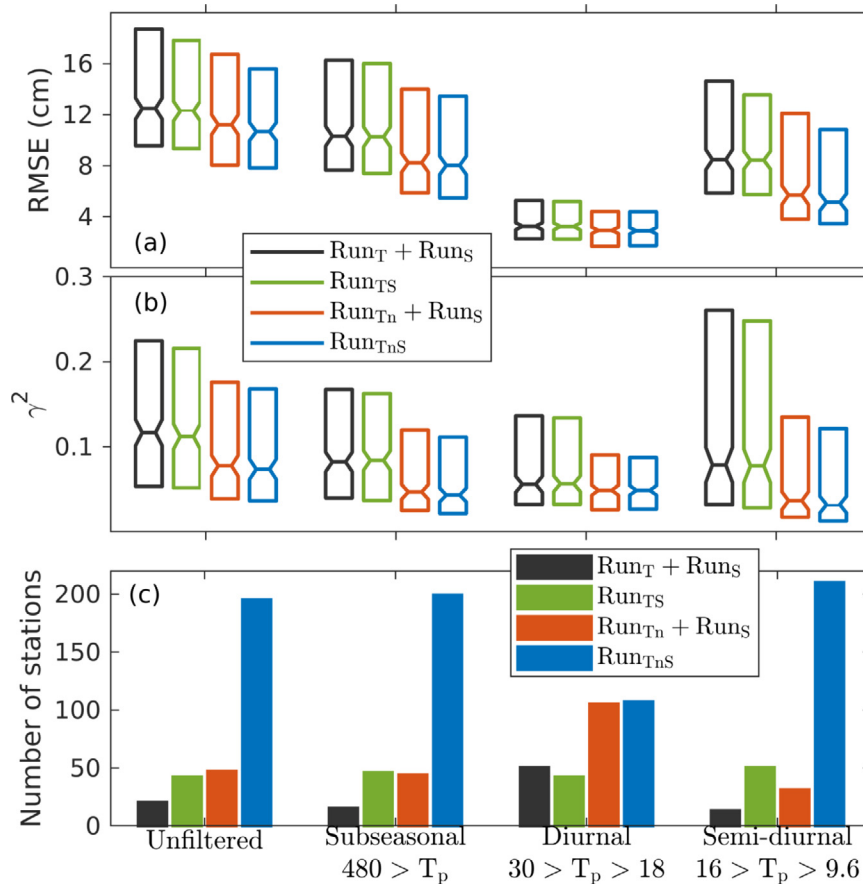
Fig. 10. Box plots, showing the three quartiles only, of (a) RMSE and (b) γ^2 for TWL produced by each prediction scheme, grouped by periods of variability. The narrowest part of the notch indicates the median and the limits of the notch indicate the 95% confidence interval. Bar plot (c) shows the number of tide gauges with the lowest RMSE, or γ^2 for each prediction scheme. The "Subseasonal" group is based on time series that were high-pass filtered with a cutoff period of 480 h. The "Diurnal" and "Semi-diurnal" groups are based on band pass filtered time series using the indicated cutoff periods (in hours).
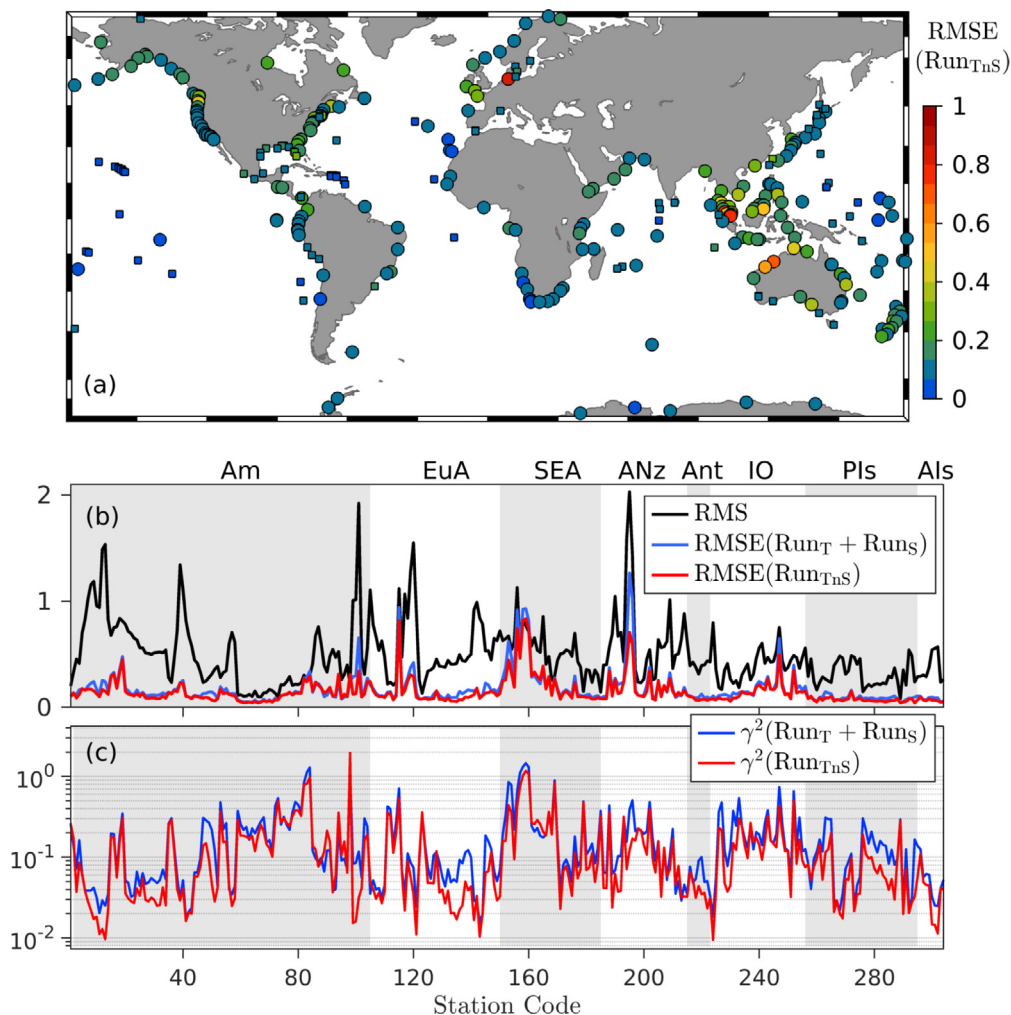
Fig. 11. Fit to the observed TWL. (a) RMSE for the coupled tide-surge run, Run_{TnS}. Squares show locations with RMS values of observed TWL below 0.3 m. (b) RMS of observed TWL (black) and RMSE for Run_{TnS} (red) and Run_T+Run_S (blue) as a function of station code (Appendix A). (c) γ^2 for Run_{TnS} and Run_T+Run_S as a function of station code. All RMS and RMSE values in m.

at exciting the global sea level response at the S_2 frequency. Decreasing the time spacing of the air pressure forcing from 1 h to 3 h reduces the S_2 amplitude in air pressure by a factor of 0.82, consistent with expectations based on Fourier analysis. A simple scaling factor does not apply if the temporal resolution is further reduced to 6 hours because the S_2 signal is aliased. Overall these results highlight the importance of using atmospheric forcing with a time spacing of one hour in order to accurately predict the global sea level response to the atmospheric S_2 tide. All of the subsequent runs used hourly atmospheric forcing.

Two "surge-only" runs, forced solely by hourly air pressure and wind stress for 2008, were performed. The original atmospheric forcing was used for Run_S. Atmospheric forcing, with its S_2 component removed, was used for $Run_{S'}$. The predicted sea levels from Run_S and $Run_{S'}$ were compared with the observed tidal residuals for the 304 tide gauges. The best fit was found for $Run_{S'}$. This is not surprising because tidal analysis of the observed TWL removes not only the gravitational S_2 tide but also the radiational S_2 component. This has implications for regional surge and TWL modeling; the radiational S_2 tide will be missed by regional models unless it is correctly represented at the model's open boundaries.

Based on runs with both atmospheric and tidal forcing (Run_{TS}, Run_{TnS}) it was shown that the radiational S_2 tide is subject to strong nonlinear interaction with the gravitational tide. The result is a pronounced attenuation of the radiational S_2 tide in large amplitude (>0.3 m) regions such as the North Sea, Patagonia Shelf and the Ross

Sea. It was shown that the attenuation can be explained by an increase in effective bottom friction at the S_2 frequency (by almost one order of magnitude in regions with large rS2) due to the presence of the gravitational tide.

Four schemes for predicting TWL were evaluated. Run_T+Run_S is the sum of separate predictions by the un-nudged tidal run and the surge run. Run_{TS} includes tide-surge interaction. $Run_{Tn}+Run_S$ and Run_{TnS} are of the same form as Run_T+Run_S and Run_{TS} but are tidally nudged. Based on comparison of model predictions with TWLs observed by the 304 tide gauges, we conclude that Run_{TnS} provides the most accurate predictions of coastal sea level. It benefits from tidal nudging in deep water leading to improved predictions of coastal tides, and nonlinear interaction between the radiational and gravitational tide leading to a significant attenuation of the radiational S_2 tide predicted by the surge-only model, Run_S. The performance of Run_{TnS} is comparable to the global reanalysis dataset provided by Muis et al. (2016) in terms of RMSE, and it compares well with the regional surge forecast system operationally operated by ECCC (Bernier and Thompson, 2015).

We note that the TPXO8 tidal solution should be reliable for prediction given the astronomical forcing can be treated as deterministic on the time scales of interest. TPXO8 can also be readily replaced by more accurate tidal solutions as they become available. A global TWL forecasting system based on the coupled tide-surge model (Run_{TnS}) is currently undergoing installation for operational use at ECCC. The system will be used to predict TWL with lead times up to 16 days and

will replace the regional deterministic system of Bernier and Thompson (2015). We are also extending this system by including baroclinicity at low computational cost, with the goal of improving the forecasts whilst keeping the computational cost sufficiently low to allow for the operational production of ensemble forecasts.

CRediT authorship contribution statement

Pengcheng Wang: Conceptualization, Methodology, Software, Validation, Formal analysis, Investigation, Writing – original draft, Writing – review & editing, Visualization. **Natacha B. Bernier:** Conceptualization, Methodology, Resources, Writing – review & editing, Supervision, Project administration, Funding acquisition. **Keith R. Thompson:** Conceptualization, Methodology, Formal analysis, Resources, Writing – review & editing. **Tsubasa Kodaira:** Methodology, Software, Funding acquisition.

Declaration of competing interest

The authors declare that they have no known competing financial interests or personal relationships that could have appeared to influence the work reported in this paper.

Acknowledgments

Appendix A. Selection and ordering of tide gauges

The locations of the tide gauges included in the present study are plotted in Fig. A.1 and listed in Table A.1. The selection, ordering and grouping of the 304 tide gauges are explained in Section 2. The table also gives the RMS of hourly observations of TWL, the corresponding RMSE and γ^2 for Run$_{TnS}$.

Appendix B. Tidal nudging

A computationally efficient method, based on Kodaira et al. (2019), is now described for nudging an ocean model toward TPXO8 observations (Section 2) in selected tidal frequency bands while allowing the model to evolve freely outside of these bands. In the present study the nudging is turned off in water shallower than 400 m (Fig. 1). This allows tide-surge and tide–tide interaction on the shelf.

Kodaira et al. (2019) implemented the method by adding a sea level nudging term of the form $\lambda\langle \eta_{obs} - \eta \rangle$ to the right side of the continuity equation, (2). However, this approach raises concern about violation of mass conservation and possible consequences for the computation of $\boldsymbol{u}$ using the momentum equation, (1). In this study we modified the approach to nudge $\boldsymbol{u}$ in the horizontal momentum equation. In this appendix we compare the effect of nudging η and $\boldsymbol{u}$.

The method is based on a recursive filter that requires only a small increase in computer memory and run time. Details of the filter and its implementation are given by Thompson et al. (2006). The filter requires specification of the centers of the tidal frequencies bands to be nudged and a parameter (κ) that controls the width of the nudged bands. The reciprocal of κ is proportional to the (e-folding) spin up time of the filter and so we define T$_{spin}= \kappa^{-1}\Delta$ where Δ is the model time step. (The tidal nudging technique is conceptually similar to applying a conventional tidal analysis over a sliding window and increasing κ is equivalent to

Table A.1
Tide gauge locations and skill of Run$_{TnS}$.

Station name	Country	Code	ID	Lon	Lat	RMS	RMSE	γ^2
North and South America (Am)								
Prudhoe Bay, AK	USA	1	579	211.47	70.40	0.20	0.10	0.26
Nome, AK	USA	2	595	194.57	64.50	0.33	0.14	0.17
Adak, AK	USA	3	40	183.37	51.86	0.46	0.09	0.04
Dutch Harbor, AK	USA	4	41	193.46	53.88	0.41	0.12	0.08
Sand Point, AK	USA	5	574	199.50	55.34	0.70	0.18	0.06
Kodiak Isl., AK	USA	6	39	207.49	57.73	0.83	0.16	0.04
Seward, AK	USA	7	560	210.57	60.12	1.02	0.17	0.03
Valdez, AK	USA	8	562	213.64	61.13	1.15	0.17	0.02
Cordova, AK	USA	9	583	214.25	60.56	1.19	0.16	0.02
Yakutat, AK	USA	10	570	220.27	59.55	0.96	0.13	0.02
Sitka, AK	USA	11	559	224.66	57.05	0.94	0.10	0.01
Ketchikan, AK	USA	12	571	228.38	55.33	1.49	0.17	0.01
Prince Rupert	CAN	13	540	229.68	54.32	1.54	0.15	0.01
Tofino	CAN	14	542	234.09	49.15	0.83	0.12	0.02
Victoria, BC	CAN	15	543	236.63	48.42	0.68	0.29	0.18
Port Angeles, WA	USA	16	584	236.56	48.13	0.75	0.31	0.17
Neah Bay, WA	USA	17	558	235.38	48.37	0.76	0.18	0.06
Willapa Bay, WA	USA	18	564	236.04	46.71	0.84	0.33	0.15
Astoria, OR	USA	19	572	236.23	46.21	0.81	0.45	0.31
South Beach, OR	USA	20	592	235.96	44.63	0.78	0.15	0.04
Charleston, OR	USA	21	575	235.68	43.35	0.72	0.13	0.03
Port Orford, OR	USA	22	557	235.50	42.74	0.69	0.12	0.03
Crescent City, CA	USA	23	556	235.82	41.74	0.65	0.11	0.03
Humboldt Bay, CA	USA	24	576	235.78	40.77	0.64	0.13	0.04
Arena Cove, CA	USA	25	573	236.29	38.91	0.56	0.10	0.03
San Francisco	USA	26	551	237.54	37.81	0.56	0.13	0.05
Monterey, CA	USA	27	555	238.11	36.61	0.51	0.09	0.03
Port San Luis, CA	USA	28	565	239.24	35.18	0.51	0.09	0.03
Harvest Oil P., CA	USA	29	594	239.33	34.47	0.50	0.09	0.03
Santa Barbara, CA	USA	30	577	240.32	34.41	0.51	0.09	0.03
Santa Monica, CA	USA	31	578	241.50	34.01	0.52	0.08	0.02
Los Angeles, CA	USA	32	567	241.73	33.72	0.52	0.08	0.03
La Jolla, CA	USA	33	554	242.74	32.87	0.51	0.11	0.04
San Diego	USA	34	569	242.83	32.71	0.54	0.09	0.03
Manzanillo	MEX	35	395	255.67	19.05	0.28	0.14	0.25
Acapulco	MEX	36	316	260.15	16.84	0.23	0.13	0.29
Acajutla	SLV	37	82	270.17	13.58	0.47	0.16	0.11
La Union	SLV	38	86	272.18	13.33	0.73	0.15	0.04
Balboa	PAN	39	302	280.43	8.97	1.34	0.23	0.03
Buenaventura	COL	40	85	282.90	3.90	1.11	0.22	0.04
Esmeraldas	ECU	41	98	280.35	0.99	0.82	0.10	0.02
Manta	ECU	42	89	279.28	−0.93	0.67	0.10	0.02
La Libertad	ECU	43	91	279.08	−2.20	0.58	0.08	0.02
Talara	PER	44	92	278.72	−4.58	0.45	0.11	0.06
Paita	PER	45	678	278.83	−5.08	0.42	0.10	0.06
Lobos de Afuera	PER	46	84	279.28	−6.93	0.34	0.09	0.07
Callao	PER	47	93	282.85	−12.05	0.24	0.09	0.14
San Juan	PER	48	96	284.80	−15.37	0.25	0.10	0.15
Matarani	PER	49	94	287.89	−17.00	0.28	0.09	0.09
Antofagasta	CHL	50	80	289.60	−23.65	0.31	0.07	0.05
Valparaiso	CHL	51	81	288.37	−33.03	0.36	0.06	0.03
Port Stanley	GBR	52	290	302.07	−51.75	0.39	0.08	0.04
Imbituba	BRA	53	718	311.60	−28.13	0.28	0.17	0.37
Ilha Fiscal	BRA	54	280	316.83	−22.90	0.33	0.13	0.15
Macae	BRA	55	719	318.53	−22.23	0.34	0.14	0.16
Salvador	BRA	56	708	321.48	−12.97	0.60	0.13	0.04
Fortaleza	BRA	57	283	321.52	−3.71	0.71	0.11	0.02
Ile Royale	FRA	58	850	307.42	5.28	0.62	0.11	0.03
Fort de France	FRA	59	271	298.95	14.58	0.11	0.06	0.29
Pointe-Pitre	FRA	60	272	298.47	16.23	0.12	0.05	0.19
Limetree Bay	USA	61	254	295.25	17.70	0.10	0.04	0.18
Lameshur Bay, VI	USA	62	214	295.28	18.32	0.11	0.04	0.18
Culebra, PR	USA	63	219	294.70	18.30	0.12	0.05	0.17
Esperanza, PR	USA	64	733	294.53	18.09	0.10	0.04	0.18
Fajardo, PR	USA	65	783	294.37	18.33	0.15	0.05	0.12
Yabucoa Harbor, PR	USA	66	734	294.17	18.06	0.10	0.05	0.19
Magueyes Island, PR	USA	67	246	292.95	17.97	0.10	0.05	0.25
Mayaguez, PR	USA	68	736	292.84	18.22	0.14	0.06	0.21
Aguadilla, PR	USA	69	263	292.84	18.46	0.14	0.05	0.14
Arecibo, PR	USA	70	735	293.30	18.48	0.17	0.06	0.13
San Juan, PR	USA	71	245	293.88	18.46	0.16	0.05	0.10

(continued on next page)

Table A.1 (*continued*).

Station name	Country	Code	ID	Lon	Lat	RMS	RMSE	γ^2
Cristobal	PAN	72	266	280.08	9.35	0.13	0.07	0.29
Puerto Moreles	MEX	73	860	273.13	20.87	0.10	0.07	0.50
Veracruz, Ver.	MEX	74	250	263.87	19.20	0.21	0.11	0.27
Port Isabel, TX	USA	75	772	262.79	26.06	0.21	0.12	0.30
Corpus Cristi, TX	USA	76	770	262.78	27.58	0.24	0.13	0.26
Galveston, P.Pier	USA	77	767	265.21	29.29	0.29	0.14	0.24
Grand Isle, LA	USA	78	765	270.04	29.26	0.21	0.12	0.32
Dauphin Island, AL	USA	79	763	271.92	30.25	0.22	0.14	0.38
Pensacola, FL	USA	80	762	272.79	30.40	0.21	0.13	0.38
Apalachicola, FL	USA	81	760	275.02	29.73	0.23	0.13	0.32
Clearwater Bch, FL	USA	82	773	277.17	27.98	0.30	0.27	0.79
St. Petersburg, FL	USA	83	759	277.37	27.76	0.27	0.24	0.81
Naples, FL	USA	84	757	278.19	26.13	0.30	0.30	0.97
Port Canaveral, FL	USA	85	774	279.41	28.42	0.41	0.15	0.14
Fernandina Beach	USA	86	240	278.53	30.67	0.68	0.24	0.12
Fort Pulaski, GA	USA	87	752	279.10	32.03	0.76	0.21	0.08
Charleston, SC	USA	88	261	280.08	32.78	0.59	0.18	0.09
Duck Pier, NC	USA	89	260	284.26	36.18	0.39	0.13	0.12
Chesapeake BBT	USA	90	749	283.89	36.97	0.33	0.15	0.21
Lewes, DE	USA	91	747	284.88	38.78	0.48	0.19	0.15
Cape May, NJ	USA	92	746	285.04	38.97	0.55	0.10	0.04
Atlantic City	USA	93	264	285.58	39.36	0.47	0.12	0.06
New York, NY	USA	94	745	285.98	40.70	0.53	0.31	0.35
Montauk, NY	USA	95	279	288.04	41.05	0.26	0.08	0.11
New London, CT	USA	96	744	287.91	41.36	0.31	0.12	0.16
Newport, RI	USA	97	253	288.67	41.51	0.40	0.10	0.06
Woods Hole, MA	USA	98	742	289.33	41.52	0.22	0.31	1.95
Boston, MA	USA	99	741	288.95	42.36	1.01	0.12	0.02
Portland, ME	USA	100	252	289.75	43.66	1.01	0.13	0.02
Eastport, ME	USA	101	740	293.02	44.90	1.92	0.34	0.03
Halifax	CAN	102	275	296.42	44.67	0.48	0.10	0.04
St. John's	CAN	103	276	307.30	47.57	0.31	0.13	0.16
Nain	CAN	104	833	298.32	56.55	0.56	0.25	0.19
Churchill	CAN	105	274	265.80	58.78	1.11	0.24	0.05

Europe and Africa (EuA)

Station name	Country	Code	ID	Lon	Lat	RMS	RMSE	γ^2
Vardo	NOR	106	805	31.10	70.33	0.78	0.16	0.04
Honningsvag	NOR	107	801	25.98	70.98	0.67	0.12	0.03
Andenes	NOR	108	800	16.15	69.32	0.54	0.10	0.04
Rorvik	NOR	109	803	11.25	64.87	0.63	0.10	0.03
Maloy	NOR	110	802	5.12	61.93	0.47	0.09	0.04
Goteborgsrsh	SWE	111	819	11.79	57.69	0.22	0.13	0.36
Hornbaek	DNK	112	838	12.47	56.10	0.24	0.13	0.32
Stockholm	SWE	113	826	18.08	59.33	0.21	0.07	0.11
Gedser	DNK	114	837	11.93	54.57	0.24	0.11	0.20
Cuxhaven	DEU	115	825	8.72	53.87	1.12	0.82	0.53
Lerwick	GBR	116	293	358.86	60.15	0.47	0.12	0.06
Stornoway	GBR	117	295	353.61	58.21	1.07	0.16	0.02
Castletownsend	IRL	118	835	350.82	51.53	0.84	0.25	0.09
Newlyn	GBR	119	294	354.46	50.10	1.28	0.31	0.06
Brest	FRA	120	822	355.50	48.38	1.55	0.29	0.04
La Coruna	ESP	121	830	351.60	43.37	0.90	0.09	0.01
Gibraltar	GBR	122	289	354.65	36.13	0.26	0.08	0.10
Marseille	FRA	123	824	5.35	43.28	0.13	0.08	0.36
Ceuta	ESP	124	207	354.68	35.90	0.24	0.09	0.13
Nouakchott	MRT	125	806	343.96	17.99	0.34	0.07	0.05
Dakar	SEN	126	223	342.58	14.68	0.35	0.08	0.05
Takoradi	GHA	127	231	358.26	4.89	0.38	0.08	0.05
Port Sonara	CMR	128	816	9.13	−4.01	0.45	0.16	0.12
Pointe Noire	COG	129	234	11.83	−4.78	0.39	0.07	0.04
Walvis Bay	NAM	130	220	14.50	−22.95	0.38	0.08	0.04
Luderitz	ZAF	131	702	15.15	−26.65	0.38	0.06	0.03
Port Nolloth	ZAF	132	701	16.87	−29.25	0.44	0.09	0.04
Saldahna Bay	ZAF	133	703	17.95	−33.02	0.41	0.06	0.02
Cape Town	ZAF	134	704	18.43	−33.90	0.41	0.06	0.02
Simon's Town	ZAF	135	221	18.43	−34.18	0.41	0.05	0.02
Mossel Bay	ZAF	136	185	22.13	−34.18	0.50	0.07	0.02
Port Elizabeth	ZAF	137	184	25.63	−33.96	0.44	0.07	0.03
East London	ZAF	138	187	27.92	−33.02	0.43	0.10	0.05
Durban	ZAF	139	181	31.05	−29.87	0.47	0.09	0.04
Richard's Bay	ZAF	140	188	32.08	−28.80	0.50	0.10	0.04
Pemba	MOZ	141	192	40.49	−12.97	0.92	0.12	0.02
Zanzibar	TZA	142	151	39.19	−6.16	0.99	0.18	0.03
Mombasa	KEN	143	101	39.66	−4.07	0.84	0.09	0.01

Table A.1 (*continued*).

Station name	Country	Code	ID	Lon	Lat	RMS	RMSE	γ^2
Lamu	KEN	144	149	40.90	−2.27	0.78	0.11	0.02
Djibouti	DJI	145	119	43.14	11.61	0.53	0.13	0.06
Aden	YEM	146	172	44.97	12.79	0.53	0.14	0.07
Salalah	OMN	147	114	54.01	16.93	0.45	0.15	0.12
Masirah	OMN	148	113	58.87	20.69	0.65	0.14	0.05
Chabahar	IRN	149	915	60.60	25.30	0.63	0.11	0.03
Karachi	PAK	150	147	66.97	24.81	0.72	0.13	0.03

Southeast Asia and Japan (SEA)

Station name	Country	Code	ID	Lon	Lat	RMS	RMSE	γ^2
Akyab	MMR	151	907	92.90	20.14	0.63	0.25	0.16
Ko Taphao Noi	THA	152	148	98.43	7.83	0.65	0.26	0.16
Langkawi	MYS	153	142	99.77	6.87	0.67	0.45	0.44
Penang	MYS	154	144	100.35	5.42	0.54	0.32	0.36
Lumut	MYS	155	143	100.61	4.24	0.62	0.19	0.09
Kelang	MYS	156	140	101.36	3.05	1.13	0.74	0.43
Keling	MYS	157	141	102.15	2.21	0.53	0.46	0.76
Kukup	MYS	158	325	103.44	1.33	0.81	0.82	1.03
Johor Baharu	MYS	159	321	103.79	1.46	0.77	0.83	1.17
Tanjong Pagar	SGP	160	699	103.85	1.26	0.71	0.74	1.08
Sedili	MYS	161	324	104.12	1.93	0.58	0.30	0.26
Tioman	MYS	162	323	104.14	2.81	0.66	0.33	0.26
Cendering	MYS	163	320	103.19	5.26	0.54	0.29	0.29
Ko Lak	THA	164	328	99.82	11.80	0.52	0.26	0.26
Vung Tau	VNM	165	383	107.07	10.34	0.86	0.39	0.21
Qui Nhon	VNM	166	381	109.26	13.78	0.41	0.17	0.19
Hong Kong	HKG	167	329	114.22	22.30	0.48	0.29	0.36
Kaohsiung	CHN	168	340	120.29	22.62	0.25	0.11	0.19
Keelung	CHN	169	341	121.75	25.16	0.29	0.27	0.83
Ishigaki	JPN	170	365	124.15	24.33	0.44	0.16	0.14
Naha	JPN	171	355	127.67	26.22	0.50	0.08	0.02
Naze	JPN	172	359	129.50	28.38	0.51	0.13	0.07
Nakano Shima	JPN	173	345	129.84	29.84	0.54	0.15	0.08
Nishinoomote	JPN	174	363	130.99	30.74	0.53	0.12	0.05
Aburatsu	JPN	175	354	131.42	31.57	0.48	0.09	0.03
Nagasaki	JPN	176	362	129.87	32.73	0.70	0.23	0.11
Kushimoto	JPN	177	353	135.78	33.47	0.43	0.10	0.05
Mera	JPN	178	352	139.83	34.92	0.38	0.10	0.07
Toyama	JPN	179	349	137.22	36.77	0.15	0.10	0.47
Ofunato	JPN	180	351	141.75	39.02	0.36	0.09	0.07
Hachinohe	JPN	181	375	141.53	40.53	0.35	0.10	0.07
Hakodate	JPN	182	364	140.73	41.78	0.23	0.08	0.11
Kushiro	JPN	183	350	144.38	42.97	0.35	0.08	0.05
Abashiri	JPN	184	347	144.28	44.02	0.31	0.09	0.09
Wakkanai	JPN	185	360	141.68	45.42	0.14	0.08	0.33

Australia and New Zealand (ANz)

Station name	Country	Code	ID	Lon	Lat	RMS	RMSE	γ^2
Port Kembla	AUS	186	342	150.91	−34.47	0.40	0.08	0.04
Fort Denison	AUS	187	333	151.23	−33.85	0.40	0.08	0.04
Brisbane	AUS	188	331	153.17	−27.37	0.57	0.34	0.36
Bundaberg	AUS	189	332	152.38	−24.77	0.69	0.11	0.02
Rosslyn Bay	AUS	190	330	150.79	−23.16	1.05	0.26	0.06
Cape Ferguson	AUS	191	343	147.06	−19.28	0.67	0.13	0.04
Townsville	AUS	192	334	146.83	−19.25	0.71	0.14	0.04
Groote Eylandt	AUS	193	145	136.42	−13.86	0.43	0.24	0.31
Darwin	AUS	194	168	130.85	−12.47	1.58	0.42	0.07
Broome	AUS	195	166	122.22	−18.00	2.03	0.71	0.12
Port Hedland	AUS	196	169	118.58	−20.32	1.44	0.59	0.17
Carnarvon	AUS	197	167	113.65	−24.90	0.36	0.14	0.16
Hillarys	AUS	198	132	115.74	−31.83	0.24	0.11	0.23
Fremantle	AUS	199	175	115.73	−32.05	0.23	0.11	0.21
Esperance	AUS	200	176	121.90	−33.87	0.27	0.10	0.14
Thevenard	AUS	201	128	133.64	−32.15	0.46	0.15	0.11
Port Stanvac	AUS	202	100	138.47	−35.11	0.54	0.34	0.40
Portland	AUS	203	129	141.61	−38.34	0.26	0.08	0.10
Spring Bay	AUS	204	335	147.93	−42.55	0.27	0.07	0.06
Bluff	NZL	205	72	168.35	−46.60	0.64	0.25	0.16
Port Chalmers	NZL	206	669	170.65	−45.82	0.56	0.10	0.03
Timaru	NZL	207	665	171.25	−44.38	0.57	0.21	0.13
Lyttelton	NZL	208	667	172.72	−43.60	0.62	0.15	0.06
Nelson	NZL	209	77	173.27	−41.27	1.01	0.27	0.07
Wellington	NZL	210	71	174.78	−41.28	0.37	0.15	0.17
Napier	NZL	211	668	176.92	−39.48	0.49	0.11	0.05
Tauranga	NZL	212	73	176.18	−37.65	0.51	0.14	0.08
Marsden Point	NZL	213	398	174.50	−35.83	0.64	0.11	0.03

Table A.1 (*continued*).

Station name	Country	Code	ID	Lon	Lat	RMS	RMSE	γ^2
Taranaki	NZL	214	76	174.03	−39.05	0.88	0.16	0.03
Jackson	NZL	215	403	168.62	−43.98	0.62	0.11	0.03
Antarctica (Ant)								
Rothera	GBR	216	832	291.87	−67.57	0.39	0.10	0.07
Faraday	ATA	217	700	295.73	−65.25	0.43	0.10	0.05
Syowa	ATA	218	127	39.60	−69.00	0.38	0.07	0.03
Mawson	AUS	219	177	62.87	−67.60	0.31	0.07	0.04
Davis	AUS	220	173	77.97	−68.45	0.39	0.07	0.03
Casey	AUS	221	130	110.53	−66.28	0.40	0.08	0.04
Dumont d'Urville	ATA	222	189	140.01	−66.66	0.44	0.07	0.02
Kerguelen	FRA	223	180	70.22	−49.35	0.43	0.08	0.03
Indian Ocean (IO)								
Dzaoudzi	FRA	224	155	45.26	−12.78	0.80	0.08	0.01
Pt. La Rue	SYC	225	121	55.53	−4.67	0.36	0.07	0.04
Reunion	FRA	226	164	55.29	−20.93	0.19	0.09	0.23
Port Louis	MRT	227	103	57.49	−20.16	0.17	0.08	0.22
Rodrigues	MRT	228	105	63.42	−19.67	0.35	0.08	0.05
Diego Garcia	GBR	229	104	72.39	−7.29	0.41	0.08	0.04
Gan	MDV	230	109	73.15	−0.69	0.27	0.06	0.04
Male, Hulule	MDV	231	108	73.53	4.19	0.23	0.09	0.15
Hanimaadhoo	MDV	232	117	73.17	6.77	0.25	0.09	0.12
Colombo	LKA	233	115	79.86	6.93	0.19	0.10	0.30
Cocos	AUS	234	171	96.90	−12.12	0.30	0.15	0.24
Christmas	AUS	235	170	105.67	−10.42	0.36	0.13	0.14
Sabang	IDN	236	123	95.32	5.89	0.41	0.13	0.10
Sibolga	IDN	237	122	98.77	1.75	0.26	0.13	0.26
Padang	IDN	238	107	100.38	−1.00	0.31	0.12	0.15
Cilicap	IDN	239	162	109.02	−7.75	0.46	0.19	0.18
Prigi	IDN	240	125	111.73	−8.28	0.56	0.21	0.14
Benoa	IDN	241	163	115.21	−8.75	0.60	0.18	0.09
Lembar	IDN	242	419	116.07	−8.73	0.42	0.16	0.16
Bintulu	MYS	243	387	113.07	3.22	0.47	0.27	0.33
Miri	MYS	244	388	113.97	4.39	0.43	0.17	0.16
Kota Kinabalu	MYS	245	386	116.07	5.98	0.43	0.17	0.15
Sandakan	MYS	246	389	118.07	5.81	0.53	0.19	0.13
Tawau	MYS	247	385	117.88	4.23	0.75	0.49	0.43
Puerto Princesa	PHL	248	380	118.73	9.75	0.44	0.20	0.19
Subic Bay	PHL	249	382	120.25	14.77	0.35	0.12	0.12
Manila	PHL	250	370	120.97	14.59	0.38	0.13	0.12
Legaspi	PHL	251	371	123.75	13.15	0.44	0.08	0.03
Cebu	PHL	252	379	123.92	10.30	0.49	0.35	0.50
Davao	PHL	253	372	125.66	7.12	0.47	0.14	0.08
Bitung	IDN	254	33	125.19	1.44	0.37	0.15	0.16
Ambon	IDN	255	133	128.20	−3.64	0.47	0.14	0.09
Saumlaki	IDN	256	420	131.29	−7.98	0.56	0.15	0.08
Pacific Islands (PIs)								
Chichijima	JPN	257	47	142.18	27.10	0.29	0.08	0.08
Malakal	PLW	258	7	134.46	7.33	0.46	0.10	0.05
Guam	USA	259	53	144.65	13.43	0.24	0.07	0.08
Pago Bay, Guam	USA	260	37	144.80	13.43	0.16	0.05	0.10
Saipan	USA	261	28	145.74	15.23	0.23	0.09	0.14
Pohnpei	FSW	262	1	158.20	6.98	0.29	0.07	0.05
Kapingamarangi	FSW	263	29	154.78	1.10	0.27	0.09	0.11
Lombrum	PNG	264	400	147.38	−2.04	0.25	0.09	0.13
Honiara	SLB	265	9	159.96	−9.42	0.23	0.10	0.20
Kwajalein	MHL	266	55	167.73	8.73	0.39	0.06	0.02
Majuro	MHL	267	5	171.37	7.11	0.43	0.07	0.03
Tarawa, Betio	KIR	268	2	172.93	1.36	0.48	0.07	0.02
Nauru	NRU	269	4	166.91	−0.53	0.46	0.06	0.02
Port Vila	VUT	270	46	168.30	−17.77	0.31	0.07	0.05
Noumea	FRA	271	19	166.42	−22.24	0.34	0.08	0.05
Lord Howe	AUS	272	399	159.07	−31.52	0.49	0.15	0.10
Lautoka	FJI	273	402	177.44	−17.61	0.47	0.07	0.02
Suva	FJI	274	18	178.43	−18.13	0.41	0.08	0.03
Funafuti	TUV	275	25	179.21	−8.50	0.46	0.09	0.04
French Frigate	USA	276	14	193.71	23.87	0.15	0.06	0.19
Nawiliwili	USA	277	58	200.65	21.97	0.19	0.06	0.11
Mokuoloe	USA	278	61	202.20	21.43	0.22	0.07	0.10
Honolulu	USA	279	57	202.13	21.31	0.20	0.06	0.10
Kaumalapau	USA	280	548	203.10	20.78	0.22	0.06	0.07
Kahului	USA	281	59	203.53	20.90	0.22	0.06	0.06

Table A.1 (*continued*).

Station name	Country	Code	ID	Lon	Lat	RMS	RMSE	γ^2
Kawaihae	USA	282	552	204.17	20.03	0.22	0.06	0.08
Hilo, Hawaii	USA	283	60	204.93	19.73	0.23	0.06	0.06
Christmas	KIR	284	11	202.53	1.98	0.22	0.05	0.05
Apia	WSM	285	401	188.25	−13.82	0.30	0.06	0.04
Pago Pago	ASM	286	56	189.32	−14.28	0.28	0.06	0.05
Nuku'alofa	TON	287	38	184.82	−21.14	0.37	0.06	0.03
Chatham	NZL	288	79	183.44	−43.95	0.26	0.08	0.10
Papeete	FRA	289	15	210.43	−17.53	0.08	0.04	0.28
Nuku Hiva	FRA	290	31	219.92	−8.93	0.35	0.05	0.02
Rikitea	FRA	291	16	225.05	−23.13	0.21	0.06	0.07
Baltra	ECU	292	3	269.72	−0.44	0.54	0.08	0.02
Santa Cruz	ECU	293	30	269.69	−0.76	0.49	0.08	0.03
San Felix	CHL	294	35	279.89	−26.29	0.24	0.04	0.03
Juan Fernandez	CHL	295	21	281.17	−33.62	0.29	0.07	0.06
Atlantic Islands (AIs)								
Bermuda	GBR	296	259	295.30	32.37	0.29	0.10	0.11
Flores, Santa Cruz	PRT	297	210	328.88	39.45	0.31	0.07	0.05
Flores, Lajes	PRT	298	213	328.83	39.38	0.29	0.06	0.05
Ponta Delgada	PRT	299	211	334.33	37.74	0.38	0.08	0.04
Funchal	PRT	300	218	343.09	32.64	0.54	0.07	0.01
Tenerife	ESP	301	228	343.76	28.48	0.56	0.07	0.01
Las Palmas	ESP	302	217	344.58	28.13	0.57	0.06	0.01
Palmeira	CPV	303	235	337.02	16.75	0.24	0.05	0.04
Ascension	GBR	304	291	345.58	−7.92	0.26	0.05	0.04

The columns are (1) station name, (2) country code following the Permanent Service for Mean Sea Level, (3) station code used in the present study, (4) UHSLC identification code, (5) longitude in degrees, (6) latitude in degrees, (7) RMS (in m) of the observed hourly TWLs for 2008, and corresponding (8) RMSE (in m) and (9) γ^2 for Run_{TnS}.

reducing the window length.) In addition to κ, it is necessary to specify the strength of the nudging, $\lambda(\boldsymbol{x})$, possibly as a function of horizontal location, $\boldsymbol{x}$.

To illustrate the use of the filter, and its sensitivity to κ, we follow Kodaira et al. (2019) and apply the filter to a simulated TWL record equal to the sum of a tide and surge component (Fig. B.1a). The tide is simulated using observed amplitudes and phases of the eight major tidal constituents for Halifax (station code 102, Table A.1). The surge is simulated using an auto-regressive model of order 1 with a realistic surge variance. Taking $T_{\text{spin}} = 14$ d allows the tides to be recovered within several cm after about $2T_{\text{spin}} = 28$ d as expected (Fig. B.1b). The surges are almost unchanged by the filter after 28 d (Fig. B.1c).

The sensitivity of the filter to different choices of κ is illustrated in Fig. B.1d. As expected, larger κ (smaller T_{spin}) gives less accurate tides due to tidal leakage from the surge. For the present application, we found that $T_{\text{spin}} = 14$ d gives acceptable results without requiring an excessively long spin up time for the filter.

B.1. Comparison of tidal nudging of sea level and current

We now compare three NEMO tidal runs subject only to gravitational forcing at the M_2 frequency. Both τ_s and p_a are set to zero. Run_T is not nudged. Run_{Tn} is nudged to $\boldsymbol{u}$ in the momentum equation and Run^*_{Tn} is nudged to η in the continuity equation (Table 1).

To quantify the effect of the nudging, the predictions of M_2 elevation are compared to TPXO8 observations (Section 2). The error is quantified by the magnitude of the difference in the complex M_2 amplitude (Z) of the observations and the colocated model predictions, $|Z_{obs} - Z_{mod}|$. This allows for errors in the timing and amplitude of the predicted tide. Following Katavouta et al. (2016), the error in tidal current is quantified by

$$\tilde{\gamma}^2 = \frac{\int_0^P |\tilde{\boldsymbol{u}}_{obs}(t) - \tilde{\boldsymbol{u}}_{mod}(t)|^2 dt}{\int_0^P |\tilde{\boldsymbol{u}}_{obs}(t)|^2 dt} \tag{B.1}$$

where P is the period of M_2 and $\tilde{\boldsymbol{u}}_{obs}(t)$ and $\tilde{\boldsymbol{u}}_{mod}(t)$ are time-varying M_2 tidal current vectors calculated from the observed and modeled tidal amplitudes and phases. Smaller $\tilde{\gamma}^2$ indicates better model performance.
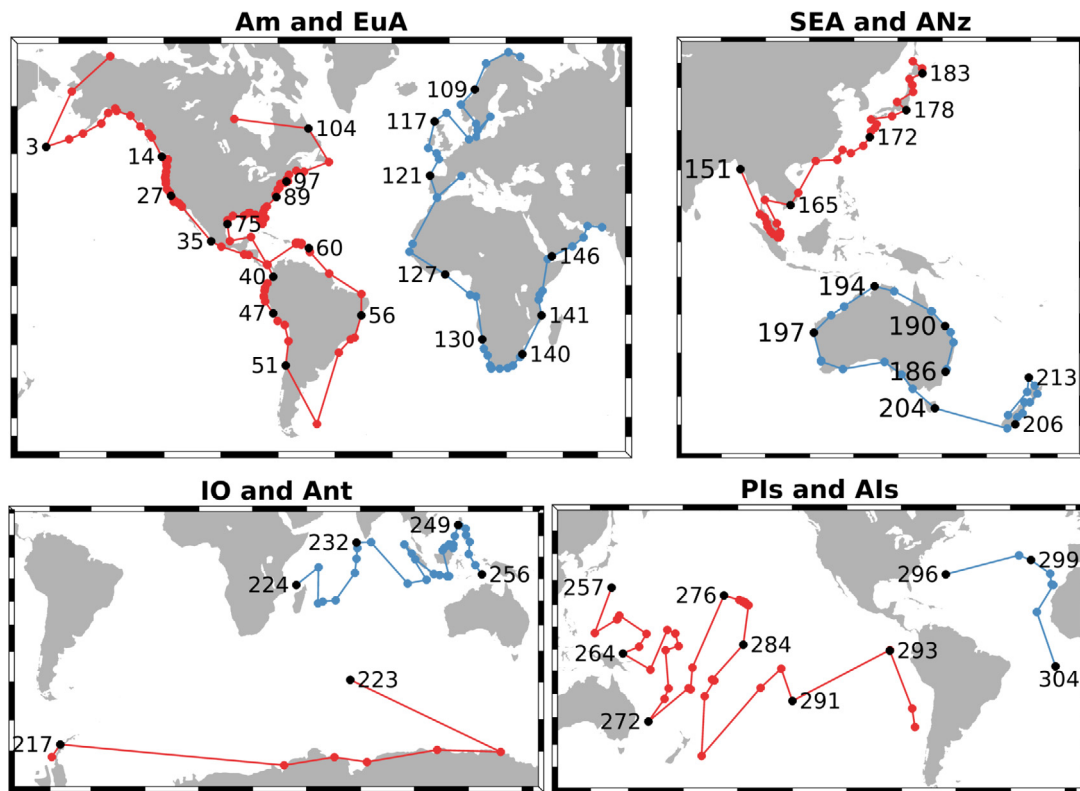
Fig. A.1. The ordered and grouped tide gauges used in the present study. The locations and codes of the 304 tide gauges are listed in Table A.1. The eight subregions, and their abbreviations, are as follows: (1) North and South America, *Am* (2) Europe and Africa, *EuA* (3) Southeast Asia and Japan, *SEA* (4) Australia and New Zealand, *ANz* (5) Indian Ocean, *IO* (6) Antarctica, *Ant* (7) Pacific Islands, *PIs* (8) Atlantic Islands, *AIs*.
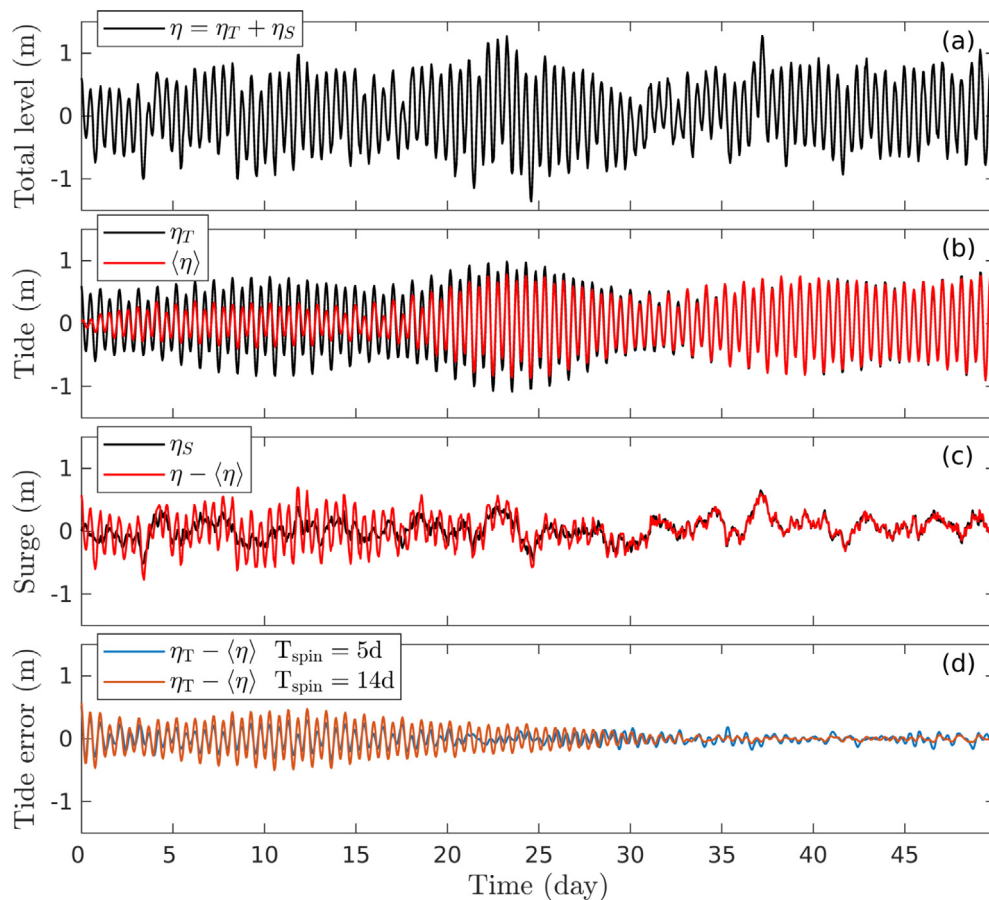

Fig. B.1. (a) Simulated total water level (η) equal to the sum of a tide (η_T) and surge (η_S) component. (b) η_T and the result of tidally filtering the total water level $\langle\eta\rangle$ assuming $T_{spin} = 14$ d. (c) η_S and the difference between η and $\langle\eta\rangle$. (d) Error in predicting the tide with $T_{spin} = 5$ d and 14 d.
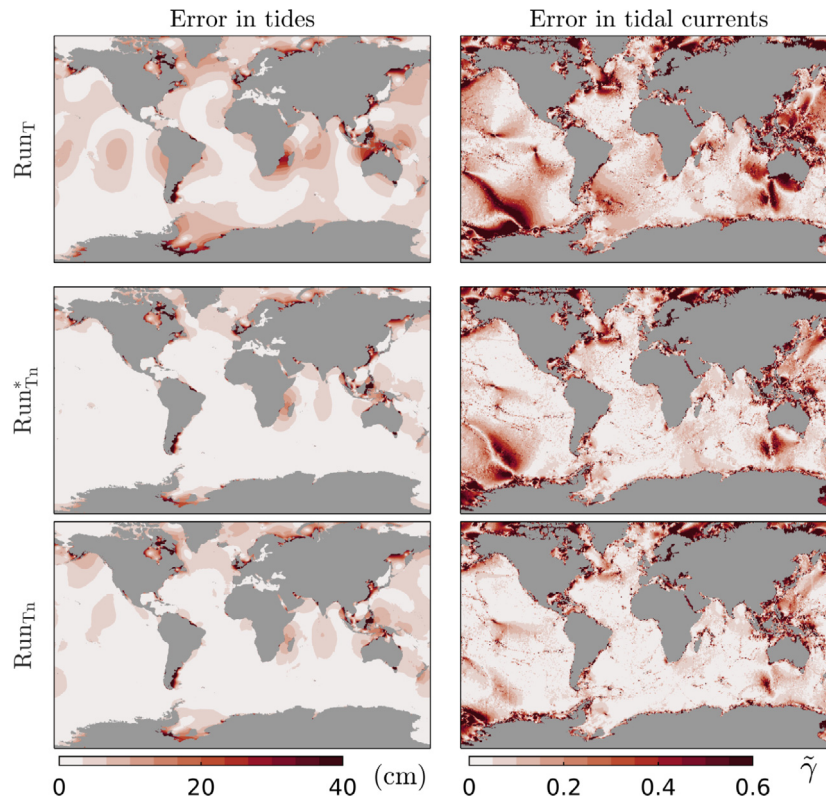
Fig. B.2. Error in predicting M_2 tidal elevation (left panels) and tidal current (right panels). The top row correspond to no nudging (Run$_T$), the middle row to nudging sea level (Run$^*_{Tn}$) and the bottom row to nudging current (Run$_{Tn}$). The error metric for elevation is $|Z_{obs} - Z_{mod}|$ and the error metric for current is $\tilde{\gamma}$ with $\tilde{\gamma}^2$ given by (B.1). See text for details. The model was fit to the TPXO8 observations.
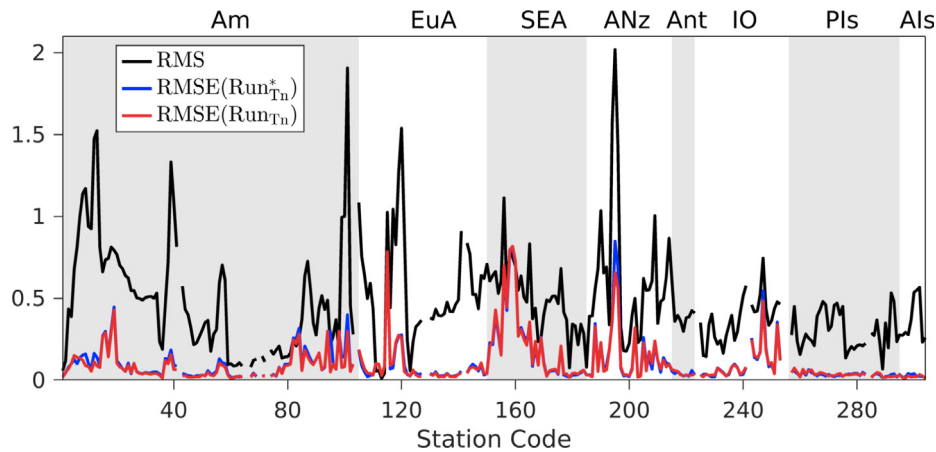
Fig. B.3. Effect of changing the nudged variable (sea level or current) on RMSE. The black line shows the RMS of tidal elevation at the 304 tide gauges based on observed M_2, S_2, N_2, K_2, O_1, K_1, P_1 and Q_1 amplitudes and phases. The blue line shows the corresponding RMSE from Run$^*_{Tn}$ (nudging sea level) and the red line shows the RMSE for Run$_{Tn}$ (nudging current). The ordering and grouping of the tide gauges is described in Appendix A. The RMS and RMSE are in m.

$\tilde{\gamma}^2$ combines errors in timing and also the length of the semi-major axis, eccentricity and orientation of the predicted tidal current ellipse.

The left panels of Fig. B.2 show that both forms of nudging result in significant improvements in M_2 tidal elevation over most of the global ocean. The improvements are not confined to the deep water where the nudging is applied (Fig. 1); improvements are also evident over the shelf, e.g., north of Australia, Mozambique Channel, and Weddell Sea. We note the nudging is not perfect and a slight degradation does occur, for example, south of Alaska for both forms of nudging. Relatively large errors remain in some regions, e.g., North Sea, Patagonia Shelf, East China Sea, Hudson Strait and Hudson Bay. We speculate higher resolution is required in these regions (Appendix C). Overall nudging

η is more effective than nudging $\mathbf{u}$. This is to be expected because Run$^*_{Tn}$ nudges η toward the TPXO8 tidal elevations.

The right panels of Fig. B.2 show both forms of nudging improve the predictions of M_2 tidal current. The improvements are comparable in the Northwest Pacific and South Atlantic Ocean. In the South Pacific, North Atlantic and Indian Ocean, nudging $\mathbf{u}$ outperforms nudging of η. This is to be expected because Run$_{Tn}$ nudges $\mathbf{u}$ toward the TPXO8 tidal currents.

In addition to the TPXO8 data, we use independent coastal sea level observations from the 304 tide gauges (Table A.1) to evaluate the two forms of nudging. The RMSE of tidal elevation predicted by Run$_{Tn}$ and Run$^*_{Tn}$ are plotted as a function of station code in Fig. B.3. The observed and predicted tides are based on the following tidal constituents: M_2,
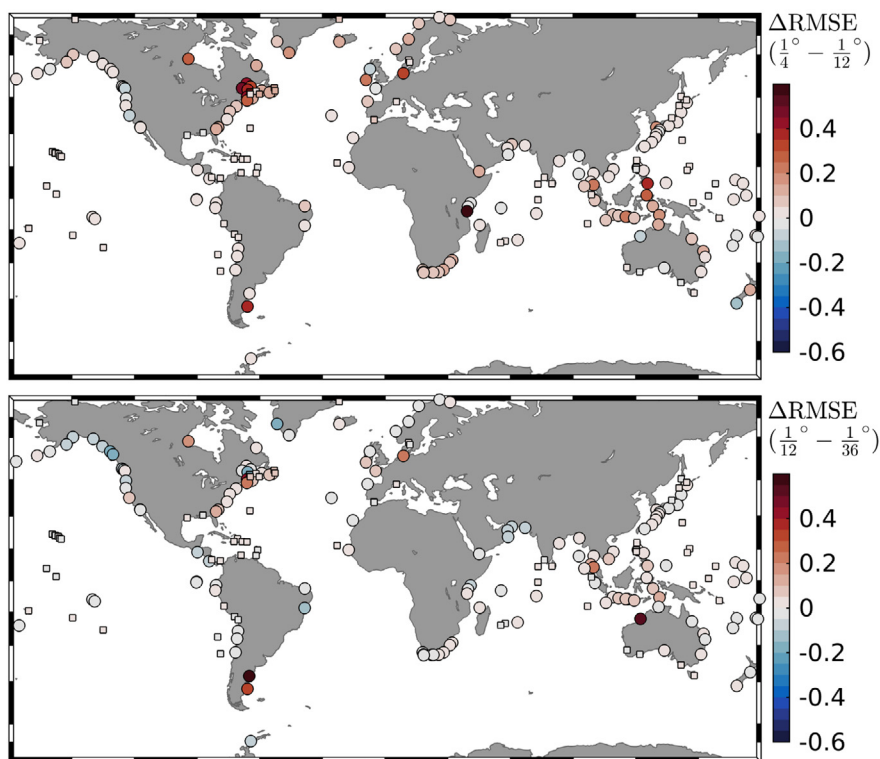
Fig. C.1. Sensitivity of tidal predictions to changes in model resolution. The upper panel shows the change in RMSE (in m) at 211 tide gauges as the model grid spacing drops from 1/4° to 1/12°. The lower panel shows the drop in RMSE as the grid spacing drops from 1/12° to 1/36°. Squares show locations where the RMS of the observed tide is below 0.3 m.

S_2, N_2, K_2, O_1, K_1, P_1 and Q_1. In order to resolve all eight constituents, this evaluation was only applied to 289 out of the 304 tide gauges with at most 50% missing observations for 2008. The RMSE is the standard deviation of the difference in the available observed and predicted hourly tides for 2008. In terms of RMSE, nudging of η and $\boldsymbol{u}$ both give an average RMSE of 0.11 m. Tidal nudging of $\boldsymbol{u}$ is more effective than nudging of η at stations in the Gulf of Maine (station code 99–101) and north of Australia (station code 194–195). Based on the above statistical analysis, and the lack of justification for violating the continuity equation, we choose to nudge $\boldsymbol{u}$ in the present study.

Appendix C. Sensitivity to model resolution

Three ORCA grids with a spacing of 1/4° (ORCA025), 1/12° (ORCA12) and 1/36° (ORCA36) are used to assess the impact of changing the horizontal resolution of the model. These three grids have a southern limit of 77° south and exclude ice cavities in the Southern Ocean in contrast to the extended grid (eORCA12) used for the main set of runs (Table 1).

The three grid sensitivity runs were all forced by GDRS forecasts of wind and air pressure. The gravitational tidal potential was evaluated at the M_2, S_2, O_1 and K_1 tidal frequencies and tidal nudging was turned off. The highest resolution bathymetry was interpolated to the coarser 1/4° and 1/12° grids. Given the high computational cost of running the model on the 1/36° grid (approximately 16 and 600 times the cost of the 1/12° and 1/4° grids, respectively), all three sensitivity runs covered a period of only 120 days. To avoid the effect of model spin up, the analysis focused on the last 90 days of each run (September 19 to December 18, 2018). As a result of the shorter analysis period, the number of observed TWL records available for model evaluation dropped from 304 to 211 (Figs. C.1 and C.2). The T_TIDE package of Pawlowicz et al. (2002) was used to decompose observed and predicted TWL into tides and surges. The surges were obtained by removing the full tidal signal from TWL and then applying a high-pass filter ($T_p < 20$ days)

to the tidal residual. The tides were reconstructed based on the four constituents (M2, S2, O1, and K1) used to force the model.

We focus first on the accuracy of the predictions of tidal elevation. Fig. C.1 shows the change in RMSE with grid spacing at the 211 tide gauges. The overall skill in predicting the tide improves significantly when the grid spacing drops from 1/4° to 1/12° (top panel). The average RMSE drops by 0.05 m (equivalent to a relative drop of 20%). The drop in RMSE exceeds 0.30 m in regions with large tides, e.g., Gulf of St. Lawrence and Bay of Fundy, North Sea, Southeast Asia and the Patagonia Shelf. Decreasing the grid spacing from 1/12° to 1/36° (bottom panel) leads to a smaller overall reduction of 0.01 m in average RMSE although reductions of 0.20–0.60 m occur in the high tide regions mentioned above. Decreasing grid spacing does not improve the fit at all stations. For example, the RMSE increases by 0.18 m at some gauges from the west coast of Canada as the spacing decreases from 1/12° to 1/36° (bottom panel).

The accuracy of the surge predictions as a function of grid spacing is illustrated in Fig. C.2. Overall, the average RMSE drops by only 4% on reducing the spacing from 1/4° to 1/12° (top panel). Reductions in RMSE of several cm are however evident in some regions, most notably the east coast of North America. Reducing the grid spacing from 1/12° to 1/36° (bottom panel) leads to negligible changes in RMSE ($\lesssim 1$ cm, see bottom panel), in agreement with Bernier and Thompson (2015). It is important to note that the evaluation of the surge predictions is being performed at tide gauges exposed to the open ocean (Section 2); much larger improvements in skill with increasing model resolution are to be expected at locations influenced by local variations in coastline and bathymetry.

Based on the above sensitivity runs, we reject the 1/4° grid spacing given its poor performance in predicting both tide and surge. Given the relatively small increase in skill, and 16 fold increase in run time, that results from decreasing the grid spacing of 1/12° to 1/36°, we will focus on 1/12°. This will allow the development of an effective 1/12° ensemble prediction system that can generate a 16 member ensemble of
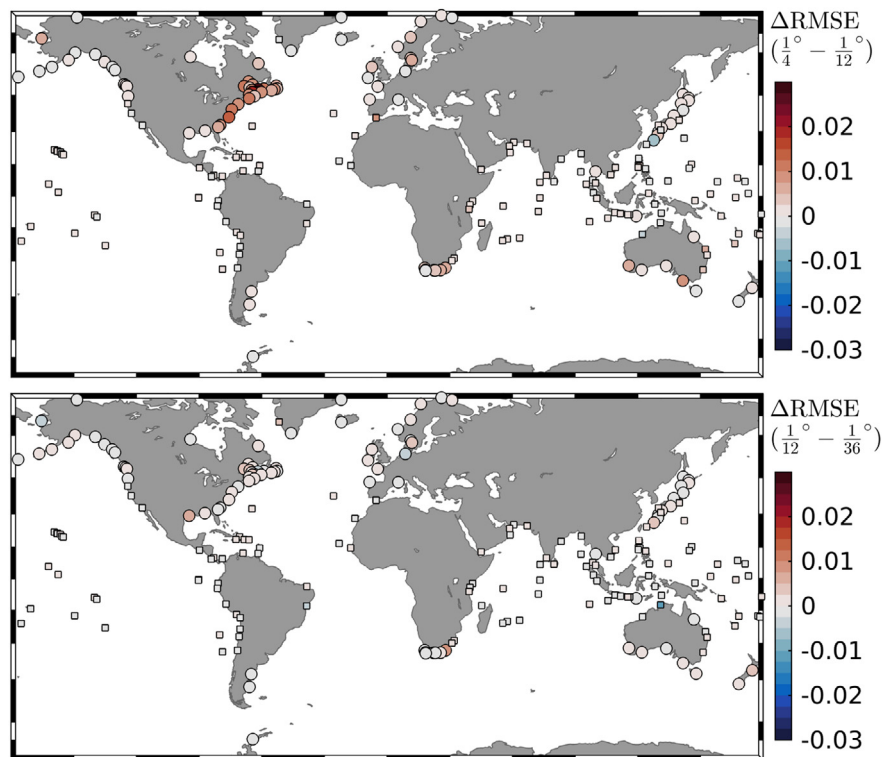
Fig. C.2. Sensitivity of surge predictions to changes in model resolution. Same format as Fig. C.1 except squares show locations where the RMS of the observed surge is below 0.05 m.

TWL predictions for about the same computational cost as a single run of the 1/36° model. This system will provide assessments of uncertainty for both operational and climate-based applications (Section 1), including the issuance of probabilistic forecasts of coastal flooding (Bernier and Thompson, 2015).

References

Allen, S., Greenslade, D., Colberg, F., Freeman, J., Schulz, E., 2018. A First-Generation National Storm Surge Forecast System. Bureau Research Report 28, Bureau of Meteorology, Melbourne, Australia, p. 86 pp.

Arbic, B.K., 2005. Atmospheric forcing of the oceanic semidiurnal tide. Geophys. Res. Lett. 32 (2), http://dx.doi.org/10.1029/2004gl021668.

Arbic, B.K., Richman, J.G., Shriver, J.F., Timko, P.G., Metzger, E.J., Wallcraft, A.J., 2012. Global modeling of internal tides: Within an eddying ocean general circulation model. Oceanography 25 (2), 20–29. http://dx.doi.org/10.5670/oceanog.2012.38.

Arbic, B.K., Wallcraft, A.J., Metzger, E.J., 2010. Concurrent simulation of the eddying general circulation and tides in a global ocean model. Ocean Model. 32 (3–4), 175–187. http://dx.doi.org/10.1016/j.ocemod.2010.01.007.

Bernier, N., Thompson, K., 2007. Tide-surge interaction off the east coast of Canada and northeastern United States. J. Geophys. Res. Oceans 112 (C6), http://dx.doi.org/10.1029/2006jc003793.

Bernier, N.B., Thompson, K.R., 2015. Deterministic and ensemble storm surge prediction for atlantic Canada with lead times of hours to ten days. Ocean Model. 86, 114–127. http://dx.doi.org/10.1016/j.ocemod.2014.12.002.

Caldwell, P., Merrifield, M., Thompson, P., 2015. Sea Level Measured by Tide Gauges from Global Oceans–The Joint Archive for Sea Level Holdings (NCEI Accession 0019568). Version 5.5, NOAA National Centers for Environmental Information, Dataset, Centers Environ. Information, p. V5V40S47W, Dataset 10.

Carrère, L., Lyard, F., 2003. Modeling the barotropic response of the global ocean to atmospheric wind and pressure forcing-comparisons with observations. Geophys. Res. Lett. 30 (6), http://dx.doi.org/10.1029/2002gl016473.

Carrère, L., Lyard, F., Cancet, M., Roblou, L., Guillot, A., 2012. FES 2012: a new tidal model taking advantage of nearly 20 years of altimetry measurements. In: Ocean Surface Topography Science Team 2012 Meeting, Venice-Lido, Italy. pp. 22–29.

Cartwright, D., 1978. Oceanic tides. Int. Hydrogr. Rev. 55 (2).

Dai, A., Wang, J., 1999. Diurnal and semidiurnal tides in global surface pressure fields. J. Atmos. Sci. 56 (22), 3874–3891.

Danard, M., Munro, A., Murty, T., 2003. Storm surge hazard in Canada. Nat. Hazards 28 (2–3), 407–434.

Davies, A., Lawrence, J., 1994. Examining the influence of wind and wind wave turbulence on tidal currents, using a three-dimensional hydrodynamic model including wave–current interaction. J. Phys. Oceanogr. 24 (12), 2441–2460.

De Kleermaeker, S., Verlaan, M., Mortlock, T., Rego, J.L., Apecechea, M.I., Yan, K., Twigt, D., et al., 2017. Global-to-local scale storm surge modelling on tropical cyclone affected coasts. In: Australasian Coasts & Ports 2017: Working with Nature. p. 358.

Dee, D.P., Uppala, S.M., Simmons, A., Berrisford, P., Poli, P., Kobayashi, S., Andrae, U., Balmaseda, M., Balsamo, G., Bauer, d.P., et al., 2011. The ERA-interim reanalysis: Configuration and performance of the data assimilation system. Q. J. R. Meteorol. Soc. 137 (656), 553–597. http://dx.doi.org/10.1002/qj.828.

Dobslaw, H., Thomas, M., 2005. Atmospheric induced oceanic tides from ECMWF forecasts. Geophys. Res. Lett. 32 (10).

Egbert, G.D., Erofeeva, S.Y., 2002. Efficient inverse modeling of barotropic ocean tides. J. Atmos. Ocean. Technol. 19 (2), 183–204.

Flowerdew, J., Horsburgh, K., Wilson, C., Mylne, K., 2010. Development and evaluation of an ensemble forecasting system for coastal storm surges. Q. J. R. Meteorol. Soc. 136 (651), 1444–1456. http://dx.doi.org/10.1002/qj.648.

Fretwell, P., Pritchard, H.D., Vaughan, D.G., Bamber, J.L., Barrand, N.E., Bell, R., Bianchi, C., Bingham, R., Blankenship, D.D., Casassa, G., et al., 2013. Bedmap2: improved ice bed, surface and thickness datasets for antarctica. Cryosphere 7 (1), 375–393.

Fu, H., Wu, X., Li, W., Zhang, L., Liu, K., Dan, B., 2021. Improving the accuracy of barotropic and internal tides embedded in a high-resolution global ocean circulation model of mitgcm. Ocean Model. 162, 101809.

Gasset, N., Fortin, V., Dimitrijevic, M., Carrera, M., Bilodeau, B., Muncaster, R., Gaborit, E., Roy, G., Pentcheva, N., Bulat, M., et al., 2021. A 10 km north american precipitation and land surface reanalysis based on the gem atmospheric model. Hydrol. Earth Syst. Sci. Discuss. 1–50.

Hallegatte, S., Green, C., Nicholls, R.J., Corfee-Morlot, J., 2013. Future flood losses in major coastal cities. Nature Clim. Change 3 (9), 802–806. http://dx.doi.org/10.1038/nclimate1979.

Han, G., Paturi, S., De Young, B., Yi, Y., Shum, C.-K., 2010. A 3-d data-assimilative tidal model of the northwest atlantic. Atmos.-Ocean 48 (1), 39–57. http://dx.doi.org/10.3137/oc303.2010.

Heaps, N.S., 1978. Linearized vertically-integrated equations for residual circulation in coastal seas. Dtsch. Hydrografische Z. 31 (5), 147–169. http://dx.doi.org/10.1007/bf02224467.

Hinkel, J., Lincke, D., Vafeidis, A.T., Perrette, M., Nicholls, R.J., Tol, R.S., Marzeion, B., Fettweis, X., Ionescu, C., Levermann, A., 2014. Coastal flood damage and adaptation

costs under 21st century sea-level rise. Proc. Natl. Acad. Sci. 111 (9), 3292–3297. http://dx.doi.org/10.1073/pnas.1222469111.

Horsburgh, K., Wilson, C., 2007. Tide-surge interaction and its role in the distribution of surge residuals in the north sea. J. Geophys. Res. Oceans 112 (C8), http://dx.doi.org/10.1029/2006jc004033.

Inoue, R., Garrett, C., 2007. Fourier representation of quadratic friction. J. Phys. Oceanogr. 37 (3), 593–610. http://dx.doi.org/10.1175/jpo2999.1.

IPCC, 2014. Summary for Policymakers. Climate Change 2014 - Impacts, Adaptation and Vulnerability: Part A: Global and Sectoral Aspects: Working Group II Contribution to the IPCC Fifth Assessment Report, Cambridge University Press, pp. 1–32.

Jayne, S.R., St. Laurent, L.C., 2001. Parameterizing tidal dissipation over rough topography. Geophys. Res. Lett. 28 (5), 811–814. http://dx.doi.org/10.1029/2000gl012044.

Katavouta, A., Thompson, K.R., Lu, Y., Loder, J.W., 2016. Interaction between the tidal and seasonal variability of the Gulf of Maine and Scotian Shelf region. J. Phys. Oceanogr. 46 (11), 3279–3298. http://dx.doi.org/10.1175/jpo-d-15-0091.1.

Kodaira, T., Bernier, N., Thompson, K.R., 2019. Application of the spectral nudging on global tides towards a global total water level prediction system. In: ASME 2019 38th International Conference on Ocean, Offshore and Arctic Engineering. American Society of Mechanical Engineers Digital Collection.

Kodaira, T., Thompson, K.R., Bernier, N.B., 2016a. The effect of density stratification on the prediction of global storm surges. Ocean Dyn. 66 (12), 1733–1743. http://dx.doi.org/10.1007/s10236-016-1003-6.

Kodaira, T., Thompson, K.R., Bernier, N.B., 2016b. Prediction of M2 tidal surface currents by a global baroclinic ocean model and evaluation using observed drifter trajectories. J. Geophys. Res. Oceans 121 (8), 6159–6183. http://dx.doi.org/10.1002/2015JC011549.

Le Provost, C., 1991. Generation of overtides and compound tides. Tidal Hydrodyn. 269–295.

Lin, H., Gagnon, N., Beauregard, S., Muncaster, R., Markovic, M., Denis, B., Charron, M., 2016. GEPS-Based monthly prediction at the Canadian meteorological centre. Mon. Weather Rev. 144 (12), 4867–4883.

Lindzen, R.S., Chapman, S., 1969. Atmospheric tides. Space Sci. Rev. 10 (1), 3–188.

Madec, G., 2008. NEMO Ocean Engine, Note du Pôle de Modélisation. Technical Report, Institut Pierre-Simon Laplace (IPSL), France, No 27, ISSN-1288-1619.

Muis, S., Verlaan, M., Winsemius, H.C., Aerts, J.C., Ward, P.J., 2016. A global reanalysis of storm surges and extreme sea levels. Nature Commun. 7, 11969. http://dx.doi.org/10.1038/ncomms11969.

Müller, M., Haak, H., Jungclaus, J., Sündermann, J., Thomas, M., 2010. The effect of ocean tides on a climate model simulation. Ocean Model. 35 (4), 304–313.

Munk, W.H., Cartwright, D.E., 1966. Tidal spectroscopy and prediction. Philos. Trans. R. Soc. Lond. Ser. A 259 (1105), 533–581.

Pawlowicz, R., Beardsley, B., Lentz, S., 2002. Classical tidal harmonic analysis including error estimates in MATLAB using T_TIDE. Comput. Geosci. 28 (8), 929–937. http://dx.doi.org/10.1016/s0098-3004(02)00013-4.

Platzman, G.W., Curtis, G.A., Hansen, K.S., Slater, R.D., 1981. Normal modes of the world ocean. Part II: Description of modes in the period range 8 to 80 hours. J. Phys. Oceanogr. 11 (5), 579–603.

Pringle, W.J., Wirasaet, D., Roberts, K.J., Westerink, J.J., 2021. Global storm tide modeling with ADCIRC v55: unstructured mesh design and performance. Geosci. Model Dev. 14 (2), 1125–1145.

Ray, R.D., Egbert, G.D., 2004. The global S1 tide. J. Phys. Oceanogr. 34 (8), 1922–1935.

Schiller, A., Fiedler, R., 2007. Explicit tidal forcing in an ocean general circulation model. Geophys. Res. Lett. 34 (3).

Stammer, D., Ray, R., Andersen, O.B., Arbic, B., Bosch, W., Carrère, L., Cheng, Y., Chinn, D., Dushaw, B., Egbert, G., et al., 2014. Accuracy assessment of global barotropic ocean tide models. Rev. Geophys. 52 (3), 243–282. http://dx.doi.org/10.1201/b18180-3.

Stepanov, V.N., Hughes, C.W., 2004. Parameterization of ocean self-attraction and loading in numerical models of the ocean circulation. J. Geophys. Res. Oceans 109 (C3), http://dx.doi.org/10.1029/2003jc002034.

Taylor, K.E., 2001. Summarizing multiple aspects of model performance in a single diagram. J. Geophys. Res.: Atmos. 106 (D7), 7183–7192.

Thompson, K.R., Sheng, J., 1997. Subtidal circulation on the Scotian Shelf: Assessing the hindcast skill of a linear, barotropic model. J. Geophys. Res. Oceans 102 (C11), 24987–25003. http://dx.doi.org/10.1029/97jc00368.

Thompson, K.R., Wright, D.G., Lu, Y., Demirov, E., 2006. A simple method for reducing seasonal bias and drift in eddy resolving ocean models. Ocean Model. 13 (2), 109–125. http://dx.doi.org/10.1016/j.ocemod.2005.11.003.

Verlaan, M., De Kleermaeker, S., Buckman, L., et al., 2015. GLOSSIS: Global storm surge forecasting and information system. In: Australasian Coasts & Ports Conference 2015: 22nd Australasian Coastal and Ocean Engineering Conference and the 15th Australasian Port and Harbour Conference. Engineers Australia and IPENZ, p. 229.

Weatherall, P., Marks, K.M., Jakobsson, M., Schmitt, T., Tani, S., Arndt, J.E., Rovere, M., Chayes, D., Ferrini, V., Wigley, R., 2015. A new digital bathymetric model of the world's oceans. Earth Space Sci. 2 (8), 331–345. http://dx.doi.org/10.1002/2015ea000107.

Werner, M., Cranston, M., Harrison, T., Whitfield, D., Schellekens, J., 2009. Recent developments in operational flood forecasting in England, Wales and Scotland. Meteorol, Appl.: J. Forecast. Pract. Appl. Train. Tech. Model. 16 (1), 13–22. http://dx.doi.org/10.1002/met.124.

Williams, J., Irazoqui Apecechea, M., Saulter, A., Horsburgh, K.J., 2018. Radiational tides: their double-counting in storm surge forecasts and contribution to the highest astronomical tide. Ocean Sci. 14 (5), 1057–1068.